

Robust Approaches to Handling Complex Geometries with Galerkin Difference Methods

Jeremy E. Kozdon^{a,*}, Lucas C. Wilcox^a, Thomas Hagstrom^b, Jeffrey W. Banks^c

^a*Department of Applied Mathematics, Naval Postgraduate School, 833 Dyer Road, Monterey, CA 93943–5216*

^b*Department of Mathematics, Southern Methodist University, PO Box 750156, Dallas, TX 75275–0156*

^c*Department of Mathematical Sciences, Rensselaer Polytechnic Institute, 110 8th Street, Troy, New York 12180.*

Abstract

The Galerkin difference (GD) basis is a set of continuous, piecewise polynomials defined using a finite difference like grid of degrees of freedom. The one dimensional GD basis functions are naturally extended to multiple dimensions using the tensor product constructions to quadrilateral elements for discretizing partial differential equations. Here we propose two approaches to handling complex geometries using the GD basis within a discontinuous Galerkin finite element setting: (1) using non-conforming, curvilinear GD elements and (2) coupling affine GD elements with curvilinear simplicial elements. In both cases the (semidiscrete) discontinuous Galerkin method is provably energy stable even when variational crimes are committed and in both cases a weight-adjusted mass matrix is used, which ensures that only the reference mass matrix must be inverted. Additionally, we give sufficient conditions on the treatment of metric terms for the curvilinear, nonconforming GD elements to ensure that the scheme is both constant preserving and conservative. Numerical experiments confirm the stability results and demonstrate the accuracy of the coupled schemes.

Keywords:

Galerkin difference methods, discontinuous Galerkin methods, high order, structure grids, curvilinear meshes, wave propagation, coupled methods

1. Introduction

The aim of this work is to propose two possible approaches to handling complex geometries in a robust and efficient manner when Galerkin difference (GD) methods are used to approximate partial differential equations. GD methods, initially proposed in [1], are element based methods where the approximation space over each element is based on a finite difference like grid of degrees of freedom. Between the grid points (called subcells below) a polynomial is built using neighboring grid values; the support of the polynomial over a subcell is finite, but the support extends beyond the subcell. It is worth noting that in general one would have many GD subcells in each GD element and the number of degrees of freedom inside an GD element is independent of the polynomial order. The GD method may be extended to multiple dimensions using a tensor product construction [2]; details of the GD approximation space are discussed in Section 4.

Since the GD method is an element based method, two-dimensional complex geometries can be handled by partitioning the domain into a set of curvilinear quadrilateral elements. Since the GD method is based on a finite difference

The views expressed in this document are those of the authors and do not reflect the official policy or position of the Department of Defense or the U.S. Government.

Approved for public release; distribution unlimited

*corresponding author

Email addresses: jekozdon@nps.edu (Jeremy E. Kozdon), lwilcox@nps.edu (Lucas C. Wilcox), thagstrom@smu.edu (Thomas Hagstrom), banksj3@rpi.edu (Jeffrey W. Banks)

like grid of degrees of freedom it is desirable to have large elements with resolution requirements handled by increasing the number of degrees of freedom within the element. This may pose a challenge for two reasons: (1) if the elements are required to be conforming (e.g., the same number of grid points are required on both sides of an element interface) unnecessarily fine grids may be required in some regions and (2) some of the cells may be so small that just having a few GD subcells inside these elements may require extremely fine grids.

To address these challenges, we propose two approaches: (1) the use of nonconforming, curvilinear GD elements and (2) coupling affine GD elements with curvilinear, polynomial simplicial elements. An example of both approaches is shown in Figure 1. In both cases, the method used is a discontinuous Galerkin method where the interelement coupling (whether GD-GD, GD-simplicial, or simplicial-simplicial) is done using numerical fluxes. The advantage of using a discontinuous Galerkin method as the underlying coupling methodology is that the resulting global mass matrix is block diagonal, which only requires the efficient inversion of elemental mass matrices.

A desirable property of any numerical method is stability. When exact integration is used, stability of the coupled method follows directly from the variational form. That said in practice, when the elements are curved, exact integration is rarely used and variational crimes can cause instability (e.g., positive real parts to the semidiscrete method's eigenvalue spectrum). In recent years skew-symmetry has been found to robustify high-order methods when the quadrature is inexact; see [3, 4, 5, 6, 7, 8, 9]. The advantage of the skew-symmetric form is that the divergence theorem (i.e., integration-by-parts) need not hold discretely for the stability analysis to follow, and the volume and surface stability are decoupled. The skew-symmetric form has also been shown to be useful even on affine elements when the mesh is nonconforming [10, 11]. The particular skew-symmetric formulation we used is based on [11]; see Section 2. An important property of the formulation is that it is provably stable even with inexact quadrature; see Section 3.

The compact support of the GD method basis functions means that the mass matrix will be banded, and thus when used in a finite element framework the inverse can be applied efficiently through a banded Cholesky factorization. Furthermore, when the element Jacobian determinant is constant (e.g., the element is affine) the mass matrix has a tensor product structure allowing a dimension-by-dimension application of the inverse along the grid lines. That said, when curved elements (or mapped geometries) are used the tensor product structure is lost and, in the naïve implementation, the full mass matrix must be factored; since the basis functions have compact support the mass matrix remains banded but the size and bandwidth are increased. Having to factor the curved mass matrix increases the initialization cost and time-stepping of the method as well as the storage requirements. To address this, we propose using a weight-adjusted mass matrix [12]. In this approach the inverse of the Jacobian weighted mass matrix is approximated in a manner that only requires the inverse of the reference mass matrix and the application of the mass matrix weighted with the reciprocal of the Jacobian determinant. We do this both for the GD elements and the curved simplicial elements, and when applied in the GD method the tensor product structure can be exploited. Details for the weight-adjusted approach are given Section 3.2.

Another important computational question is the storage of the metric terms. As will be seen when the metric terms are non-constant a set of GD quadrature nodes must be used. This grid of quadrature nodes is fine compared with the GD grid of degrees of freedom since many quadrature nodes are needed over each GD subcell. If the metric terms are stored at the quadrature nodes then the storage requirements are drastically increased, thus we propose computing the L^2 -projection of the metric terms to the GD approximation space. Furthermore, we also show how the metric terms can be computed across non-conforming curved interfaces so that the scheme is both conservative and constant preserving; see Section 4.3.

In the remainder of the text, we will use linear acoustics as a model problem with constant material properties. The approach can be extended to any linear equation with has a skew-symmetric formulation.

2. Model Problem and Skew Symmetric Discontinuous Galerkin Scheme

For our model problem, we consider the two-dimensional, constant coefficient acoustic wave equation in first order form:

$$\frac{\partial p}{\partial t} + \nabla \cdot \mathbf{v} = 0, \quad \frac{\partial \mathbf{v}}{\partial t} + \nabla p = \mathbf{0}, \quad \text{in } \Omega, \quad (1)$$

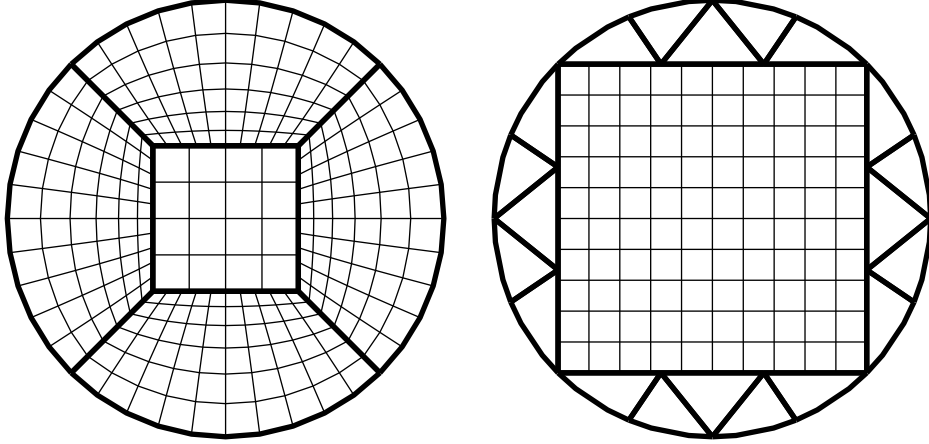


Figure 1: Example domain decompositions for two approaches to handling complex geometries with GD methods. The thick lines show the boundaries of the elements and the thin lines show the GD grid lines (i.e., subcell boundaries). (left) A decomposition with curved GD elements. (right) A decomposition with an affine GD element and several curved simplicial elements.

where p is the pressure and $\mathbf{v} = [v_x \ v_y]^T$ is the particle velocity in the x and y directions. Here $\Omega \subset \mathbb{R}^2$ is the domain of the problem. For simplicity, only periodic and the zero normal velocity boundary condition,

$$\mathbf{n} \cdot \mathbf{v} = 0 \quad \text{on} \quad \partial\Omega, \quad (2)$$

are considered. In (2) \mathbf{n} is the outward pointing unit normal to $\partial\Omega$.

The discontinuous Galerkin (DG) discretization of the acoustic wave equation begins with a partition of the domain into a set, \mathcal{E} , of non-overlapping elements such that $\Omega = \bigcup_{e \in \mathcal{E}} e$. Following [11], we allow the elements to be non-conforming by patching them together with a mortar, $\Gamma = \bigcup_{e \in \mathcal{E}} \partial e$, where ∂e is the boundary of element e . The mortar is partitioned into a set, \mathcal{G} , of non-overlapping, one-dimensional mortar elements such that $\Gamma = \bigcup_{g \in \mathcal{G}} g$ and each mortar element intersects at most the boundary of two elements. The set of mortar elements that a volume element $e \in \mathcal{E}$ connects to is

$$\mathcal{G}^e = \{g \in \mathcal{G} \mid g \cap \partial e \neq \emptyset\}. \quad (3)$$

For each element, $e \in \mathcal{E}$, we assume there exists a diffeomorphic mapping from the reference element \hat{e} to e . We let $\{x^e(r, s), y^e(r, s)\}$ be this mapping and $\{r^e(x, y), s^e(x, y)\}$ be its inverse. Likewise, for each mortar element, $g \in \mathcal{G}$, we assume there exists a diffeomorphic mapping from the reference element \hat{g} to g . We let $\{x^g(r), y^g(r)\}$ be this mapping and $\{r^g(x, y), s^g(x, y)\}$ be its inverse.

Let V_h^e be a finite-dimensional approximation space over \hat{e} . Below, depending on the type of element, this is the span of a Galerkin difference (GD) basis, described in Section 4, or the span of polynomials up to a given order.

The division of the mortar and the approximation space for each reference mortar element are chosen to represent the trace of functions from V_h^e exactly. Depicted in Figure 2 is how the mortar space would be partitioned when two GD elements are connected (left panel) and a single GD element connects to several simplicial elements (right panel). The thick lines denote interfaces between elements and the thin lines denote subcells of the larger GD element that support a single tensor product polynomial in the reference space (see Section 4 for more detail on the GD basis). Each side of a mortar element connects to either a single GD subcell or simplicial element. The approximation space for the reference mortar element, \hat{g} , is the space of one-dimensional polynomials of degree less than or equal to n , denoted \mathbb{P}_n , with n being the maximum polynomial order on the two-sides of the mortar.

A skew-symmetric discontinuous Galerkin semi-discretization of (1) is: For each element $e \in \mathcal{E}$ find a $p \in$

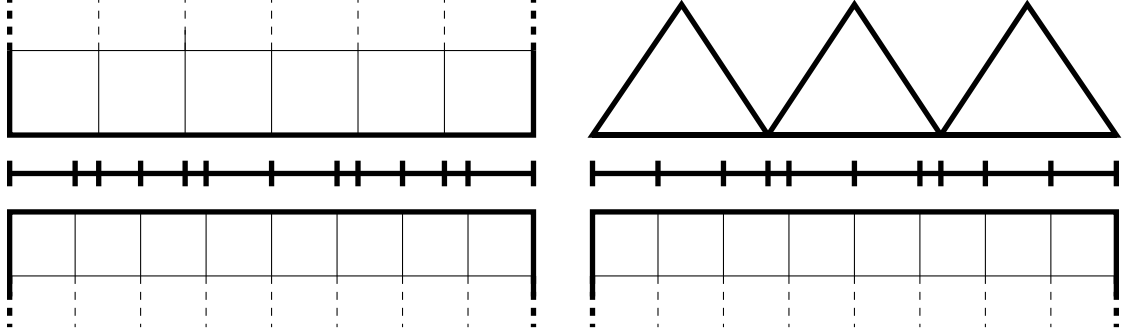


Figure 2: Mortar elements that would be used to connect two GD elements (left) and a GD element with several simplicial elements (right). The elements have been separated vertically to show the mortar elements, which are represented by the hash marks on the line between the elements. In both panels the dashed line indicates that the GD element has been truncated and the thin lines show the GD grid lines (i.e., subcell boundaries). In the right panel only elements that connect to the GD element are shown and mortar elements between simplicial elements are not shown.

$[0, T] \times V_h^e$ and $\mathbf{v} \in ([0, T] \times V_h^e)^2$ such that

$$\int_{\hat{e}} \left(J\phi \frac{\partial p}{\partial t} + J\phi \nabla \cdot \mathbf{v} \right) = - \sum_{g \in \mathcal{G}^e} \int_{\partial \hat{g}} S_J^g \phi^- (v_n^* - v_n^-), \quad (4)$$

$$\int_{\hat{e}} \left(J\omega^T \frac{\partial \mathbf{v}}{\partial t} - J(\nabla \cdot \omega) p \right) = - \sum_{g \in \mathcal{G}^e} \int_{\partial \hat{g}} S_J^g \omega_n^- p^*, \quad (5)$$

for all $\phi \in V_h^e$ and $\omega \in (V_h^e)^2$. Here ϕ^- denotes the trace of the volume element field ϕ on the mortar element g . Likewise $v_n^- = \mathbf{n}^- \cdot \mathbf{v}^-$ and $\omega_n^- = \mathbf{n}^- \cdot \omega^-$ where \mathbf{n}^- is the outward pointing normal of element e . The volume and surface Jacobian determinants are J and S_J^g , respectively. The terms p^* and v_n^* are the numerical fluxes, which couple the solution across the element interfaces and are defined as

$$p^* = \{p\} - \frac{\alpha}{2} \llbracket v_n \rrbracket, \quad v_n^* = \{v_n\} - \frac{\alpha}{2} \llbracket p \rrbracket, \quad (6)$$

for some constant $\alpha \geq 0$. Here $\{p\} = (p^+ + p^-)/2$ is the average and $\llbracket p \rrbracket = p^+ - p^-$ is the jump across the mortar with p^- denoting the trace of p from e on g and p^+ the trace from the other element connected on g . At the outer boundaries, the zero velocity boundary condition is enforced by setting $p^+ = p^-$ and $v_n^+ = -v_n^-$.

3. Semi-Discrete Scheme

In this section we define a quadrature-based discretization of (4)–(5) as well as introduce the matrix vector form of the problem (17)–(19). To start with we leave the notation fairly general so that it includes both the (yet to be defined) GD elements and simplicial elements; details of the specific choices for each of these operators is given later in the text for the GD basis. We refer the reader to Hesthaven and Warburton [13] for a detailed description of the polynomial basis for simplicial elements. In what follows we describe the operators from the perspective of a single element. These operators can vary from element to element depending on the element type and metric terms. That said, in order to simplify the notation we suppress any superscripts or subscripts to denote element unless this is needed for clarity, for instance when discussing mortar elements.

Let $\{\phi_k\}_{k=0}^N \in V_h^e$ be a basis for the reference space of element e . Thus, any function $q \in V_h^e$ can be represented as

$$q = \sum_{k=0}^N q_k \phi_k = \boldsymbol{\phi}^T \mathbf{q}, \quad (7)$$

with $\mathbf{q} = [q_0 \dots q_N]^T$ and $\boldsymbol{\phi} = [\phi_0 \dots \phi_N]^T$. We approximate integrals over reference element \hat{e} with the N_q -point, positive weight, interpolatory quadrature rule

$$\int_{\hat{e}} f \approx \sum_{k=1}^{N_q} \omega_k f(r_k, s_k), \quad (8)$$

where the quadrature weights $\{\omega_k\}_{k=1}^{N_q}$ are strictly positive and quadrature node locations $\{(r_k, s_k)\}_{k=1}^{N_q}$ are given for the reference element. Inner products of $p, q \in V_h^e$ weighted by $J \in L^2(\hat{e})$ can then be approximated as

$$\int_{\hat{e}} J p q \approx \sum_{k=1}^{N_q} \omega_k J(r_k, s_k) p(r_k, s_k) q(r_k, s_k) = \mathbf{p}^T \mathbf{L}^T \mathbf{W} \mathbf{J} \mathbf{L} \mathbf{q}, \quad (9)$$

where \mathbf{W} is a diagonal matrix of the quadrature weights, \mathbf{J} is a diagonal matrix of J evaluated at the quadrature nodes, and \mathbf{L} interpolates functions in V_h^e which have been expanded in basis $\boldsymbol{\phi}$ to the integration nodes. For convenience, we define the J -weighted mass matrix to be

$$\mathbf{M}_J = \mathbf{L}^T \mathbf{W} \mathbf{J} \mathbf{L}. \quad (10)$$

Since the quadrature weights are positive and the nodes are distinct, the mass matrix \mathbf{M}_J is symmetric positive definite as long as $J > 0$ at the quadrature nodes and $N \leq N_q$, i.e., there are more quadrature nodes than basis functions for the space V_h^e .

We let \mathbf{D}_r and \mathbf{D}_s be operators that differentiate functions in V_h^e that have been expanded in basis $\boldsymbol{\phi}$ in the reference directions r and s , respectively. These operators evaluate the derivatives at the quadrature nodes. Letting $p, v_x, v_y \in V_h^e$ with $\mathbf{v} = [v_x \ v_y]^T$ we then have the following approximation:

$$\begin{aligned} \int_{\hat{e}} J p \nabla \cdot \mathbf{v} &= \int_{\hat{e}} J p \left(\frac{\partial v_x}{\partial x} + \frac{\partial v_y}{\partial y} \right) = \int_{\hat{e}} J p \left(\frac{\partial r}{\partial x} \frac{\partial v_x}{\partial r} + \frac{\partial s}{\partial x} \frac{\partial v_x}{\partial s} + \frac{\partial r}{\partial y} \frac{\partial v_y}{\partial r} + \frac{\partial s}{\partial y} \frac{\partial v_y}{\partial s} \right) \\ &\approx \mathbf{p}^T \mathbf{L}^T \mathbf{W} \mathbf{J} (\mathbf{r}_x \mathbf{D}_r \mathbf{v}_x + \mathbf{s}_x \mathbf{D}_s \mathbf{v}_x + \mathbf{r}_y \mathbf{D}_r \mathbf{v}_y + \mathbf{s}_y \mathbf{D}_s \mathbf{v}_y). \end{aligned} \quad (11)$$

Here \mathbf{r}_x is a diagonal matrix of $\partial r / \partial x$ evaluated at the quadrature nodes, with similar definitions for \mathbf{s}_x , \mathbf{r}_y , and \mathbf{s}_y . It is convenient to define the stiffness matrices

$$\mathbf{S}_x = \mathbf{L}^T \mathbf{W} \mathbf{J} (\mathbf{r}_x \mathbf{D}_r + \mathbf{s}_x \mathbf{D}_s), \quad \mathbf{S}_y = \mathbf{L}^T \mathbf{W} \mathbf{J} (\mathbf{r}_y \mathbf{D}_r + \mathbf{s}_y \mathbf{D}_s), \quad (12)$$

so that we can write (11) as

$$\int_{\hat{e}} J p \nabla \cdot \mathbf{v} \approx \mathbf{p}^T (\mathbf{S}_x \mathbf{v}_x + \mathbf{S}_y \mathbf{v}_y). \quad (13)$$

Integrals over mortar element $g \in \mathcal{G}^e$ are approximated using the N_q^g -point, positive weight, interpolatory quadrature rule

$$\int_{\hat{g}} f \approx \sum_{k=1}^{N_q^g} \omega_k^g f(r_k^g), \quad (14)$$

where $\{\omega_k^g\}_{k=1}^{N_q^g}$ and $\{r_k^g\}_{k=1}^{N_q^g}$ are the surface quadrature weights and nodes, respectively. The S_J^g -weighted inner product of functions $\bar{p}, \bar{q} \in \mathbb{P}_N$ over \hat{g} is approximated by

$$\int_{\hat{g}} S_J^g \bar{p} \bar{q} \approx \sum_{k=1}^{N_q^g} \omega_k^g S_J^g(r_k^g) \bar{p}(r_k^g) \bar{q}(r_k^g) = \bar{\mathbf{p}}^T \mathbf{S}_J^g \mathbf{W}^g \bar{\mathbf{q}}, \quad (15)$$

where \mathbf{W}^g is a diagonal matrix of the quadrature weights, \mathbf{S}_J^g is a diagonal matrix of S_J^g evaluated at the quadrature nodes, and vectors $\bar{\mathbf{p}}$ and $\bar{\mathbf{q}}$ are \bar{p} and \bar{q} evaluated at the quadrature nodes. Evaluation of mortar integrals involving

the trace of $p, q \in V_h^e$ on the mortar (e.g., p^- and q^-) can be evaluated by defining the matrix \mathbf{L}^g as the interpolation matrix from \hat{e} to the quadrature nodes over \hat{g} . With this we then have the integral approximation

$$\int_{\hat{g}} S_J^g p^- q^- \approx \mathbf{p}^T (\mathbf{L}^g)^T S_J^g \mathbf{W}^g \mathbf{L}^g \mathbf{q}. \quad (16)$$

For stability, the same surface Jacobian determinant must be used for the volume update on both sides of the mortar. Since the mortar element space need not be a subspace of the trace of the volume element space, the representation of the surface Jacobian determinant on mortar element g may be different than the representation of surface Jacobian determinant on the connected face of element e . For GD elements this is important, since the only functions that can be represented exactly on both side of a nonconforming GD interface are polynomials (as opposed to piecewise polynomials); see [11] for a fuller discussion of the mortar elements.

With this notation, a skew-symmetric quadrature based version of (4)–(5) is then: For each $e \in \mathcal{E}$ find a $p, v_x, v_y \in V_h^e([0, T] \times V_h^e)$ such that

$$\mathbf{M}_J \frac{d\mathbf{p}}{dt} + S_x v_x + S_y v_y = - \sum_{g \in \mathcal{G}^e} (\mathbf{L}^g)^T S_J^g \mathbf{W}^g (v_n^* - v_n^-), \quad (17)$$

$$\mathbf{M}_J \frac{dv_x}{dt} - S_x^T \mathbf{p} = - \sum_{g \in \mathcal{G}^e} (\mathbf{L}^g)^T \mathbf{n}_x^{-g} S_J^g \mathbf{W}^g \mathbf{p}^*, \quad (18)$$

$$\mathbf{M}_J \frac{dv_y}{dt} - S_y^T \mathbf{p} = - \sum_{g \in \mathcal{G}^e} (\mathbf{L}^g)^T \mathbf{n}_y^{-g} S_J^g \mathbf{W}^g \mathbf{p}^*. \quad (19)$$

Here \mathbf{n}_x^{-g} and \mathbf{n}_y^{-g} are diagonal matrices of the components of the unit normal to mortar g evaluated at the mortar element quadrature points; the normal is defined to be outward with respect to element e . Note, it is important for stability that the normal used for the element on the opposite side of the mortar be equal in magnitude but opposite in sign. The normal velocity on the mortar is defined to be

$$v_n^- = \mathbf{n}_x^{-g} \mathbf{L}^g v_x + \mathbf{n}_y^{-g} \mathbf{L}^g v_y. \quad (20)$$

The flux vectors \mathbf{p}^* and v_n^* are defined by applying (6) pointwise.

We again note that scheme (17)–(19) is written from the point of view of a single element e , and each element e will have unique solution vectors and matrices (e.g., in general the mass matrix and stiffness matrices are different for each element).

3.1. Energy stability

Let the energy in element e be defined as

$$\mathcal{F}^e = \frac{1}{2} (\mathbf{p}^T \mathbf{M}_J \mathbf{p} + v_x^T \mathbf{M}_J v_x + v_y^T \mathbf{M}_J v_y). \quad (21)$$

Then, the energy in the whole domain is

$$\mathcal{F} = \sum_{e \in \mathcal{E}} \mathcal{F}^e. \quad (22)$$

If \mathbf{M}_J is symmetric positive definite for all $e \in \mathcal{E}$, it follows that \mathcal{F} is a well-defined norm of the solution. With this and the restriction that S_J^g is positive for all mortar elements, we have the following stability result.

Theorem 3.1. *The semidiscrete scheme (17)–(19) satisfies the energy estimate $\mathcal{F}(t) \leq \mathcal{F}(0)$ for $t > 0$.*

Proof. See Appendix Appendix A. □

3.2. Weight-Adjusted DG

One of the computational challenges with (17)–(19) is that \mathbf{M}_J must be inverted. In practice this means that different factors of \mathbf{M}_J will be needed for each element which drastically increases the storage costs of the method. As will be seen, when the GD basis is used on affine elements the mass matrix has a tensor product (dimension-by-dimension) structure which allows for the efficient application of its inverse. However, when the Jacobian determinant is non-constant this tensor product structure is lost and the full two-dimensional mass matrix must be factored.

To overcome this computational challenge, we propose using the weight-adjusted approach of Chan, Hewett, and Warburton [12]. In this approach the mass matrix is approximated as $\mathbf{M}_J \approx \mathbf{M}\mathbf{M}_{1/J}^{-1}\mathbf{M}$. To apply the inverse of this approximation, one only needs to multiply by the mass matrix weighted by the $1/J$ and the inverse of the reference element mass matrix \mathbf{M} . For GD elements the action of \mathbf{M}^{-1} can be efficiently applied in tensor product form; efficiency on simplicial elements comes from the fact that they all have the same reference mass matrix (and thus factors).

This weight-adjusted approximation of \mathbf{M}_J is arrived at by approximating multiplication by J with the operator $T_{1/J}^{-1}$:

$$\int_{\hat{e}} J\phi u \approx \int_{\hat{e}} \phi T_{1/J}^{-1} u. \quad (23)$$

Let $u \in V_h^e$, then $T_{1/J}^{-1}u \in V_h^e$ is defined by

$$\int_{\hat{e}} \phi \frac{1}{J} T_{1/J}^{-1} u = \int_{\hat{e}} \phi u, \quad (24)$$

for all $\phi \in V_h^e$. To see how this gives rise to the weight-adjusted mass matrix above, we first define $u_J = T_{1/J}^{-1}u$ which allows us to write

$$\int_{\hat{e}} \phi T_{1/J}^{-1} u = \phi^T \mathbf{M} u_J. \quad (25)$$

The quantity u_J is calculated using (24):

$$\phi^T \mathbf{M}_{1/J} u_J = \phi^T \mathbf{M} u. \quad (26)$$

Since $\phi \in V_h^e$ is arbitrary we then have that

$$u_J = \mathbf{M}_{1/J}^{-1} \mathbf{M} u. \quad (27)$$

Substituting this back into (25), gives the weight-adjusted mass matrix:

$$\int_{\hat{e}} \phi T_{1/J}^{-1} u = \phi^T \mathbf{M} \mathbf{M}_{1/J}^{-1} \mathbf{M} u. \quad (28)$$

Typically $\mathbf{M}_{1/J}$ will not be an exact mass matrix since both J and $1/J$ will be approximated and inexact quadrature is used. With the assumption that $\mathbf{M}_{1/J}$ is symmetric positive definite, the stability properties of the scheme remain unchanged.

We thus have the following corollary to Theorem 3.1

Corollary 3.1. *The semidiscrete scheme (17)–(19) with the weight-adjusted mass matrix satisfies the energy estimate $\mathcal{F}(t) \leq \mathcal{F}(0)$ for $t > 0$.*

4. Galerkin Difference Basis

Galerkin difference methods [1, 2] are Galerkin finite elements methods built using basis functions defined on a grid of degrees of freedom similar to a finite difference method. The key feature of a GD basis is that the basis functions have compact support on the grid, which results in banded element mass and stiffness matrices. We begin by describing the GD approximation in one dimension and then discuss the generalization to multiple dimensions.

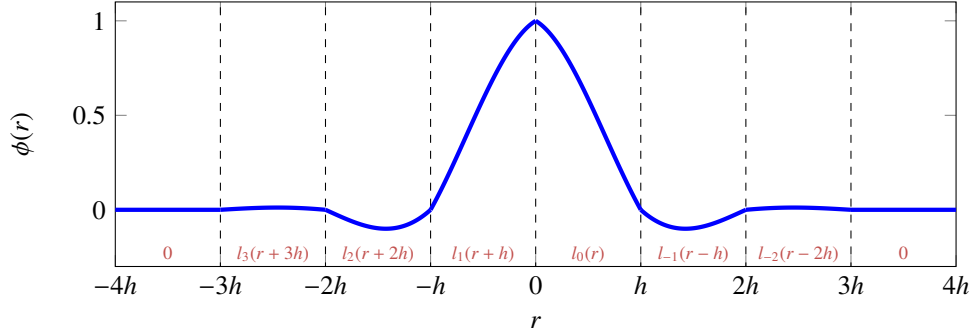


Figure 3: Example of $\phi(r)$ for $n = 5$ ($m = 3$). The equations at the base of the figure give the Lagrange polynomial used over the interval, which are denoted by the dashed lines.

4.1. One-Dimensional Galerkin Difference Basis Functions

Consider the domain $[-1, 1]$ discretized with $N + 1$ grid equally spaced points. The spacing between the grid points is $h = 2/N$ and the location of grid point i is $r_i = ih - 1$, for $i = 0, \dots, N$. Over each interval $R_i = [r_i, r_{i+1}]$ a polynomial of degree $n = 2m - 1$ is built using values at $2m$ grid points centered around R_i ; we call these intervals subcells.

Consider a subcell R_i sufficiently far from the boundary, i.e., $i \geq m - 1$ and $i \leq N - m$. In the subcell it is natural to use a symmetric stencil to construct the polynomial, namely values from grid points $\{i + 1 - m, i + 2 - m, \dots, i + m\}$. Thus, if $r \in R_i$ the GD approximation of a function u would be

$$u(r) = \sum_{k=1-m}^m u_{i+k} l_k(r - ih), \quad (29)$$

where u_{i+k} are the GD grid point values. These values can be defined in a number of ways, such as through interpolation $u_i = u(r_i)$ or an L^2 projection of u onto the GD approximation space. Here, $l_k(r)$ is the n th order Lagrange interpolating polynomial that satisfies $l_k(jh) = \delta_{jk}$ for $j = 1 - m, \dots, m$. We say that a function of the form (29) is in the space $W_{N,n}$ where $n = 2m - 1$. This construction of the GD approximation implies that it is continuous and its derivative is discontinuous between subcells.

Near the boundary there are several options for how to define the approximation. One option is to use (29) but allow some degrees of freedom to be outside of the domain. Namely, the left-most degree of freedom would be $r_{1-m} = -1 - (m - 1)h$ and the right-most $r_{N+m-1} = 1 + (m - 1)h$. This is the so-called *ghost basis* method [1]. Another option is to bias the stencil toward the interior and use a non-symmetric stencil to construct the approximation near the boundary. This can be done by either modifying the interpolation formula for $u(r)$ near the boundary or by using (29) near the boundary with points outside the domain filled using extrapolation. This second approach is called the *extrapolation* method [1]. A third option would be to use a mixture of the two methods with some nodes outside the domain being ghost basis nodes and other nodes being extrapolated.

Regardless of whether the ghost basis or extrapolated boundary closure is used, linearity and compactness of the interpolant allows us to define the global interpolant as

$$u = \sum_{k=1-m}^{N+m-1} u_k \phi_k. \quad (30)$$

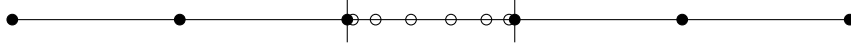


Figure 4: The solid dots are the GD grid points (degrees of freedom) that would be used to build an interpolant over the center interval (indicated with the vertical lines) if $m = 3$, i.e., polynomial order over the interval is $n = 5$. The open dots show the 6 Legendre–Gauss nodes that would be used to integrate the inner product of two GD interpolants.

Here the k th basis function is defined as $\phi_k(r) = \phi(r + 1 - kh)$, where

$$\phi(r) = \begin{cases} 0, & \text{if } r \leq -mh, \\ l_m(r + mh), & \text{if } -mh < r \leq -(m-1)h, \\ l_{m-1}(r + (m-1)h), & \text{if } -(m-1)h < r \leq -(m-2)h, \\ \vdots \\ l_{2-m}(r + (2-m)h), & \text{if } (m-2)h < r \leq (m-1)h, \\ l_{1-m}(r + (1-m)h), & \text{if } (m-1)h < r \leq mh, \\ 0, & \text{if } mh < r. \end{cases} \quad (31)$$

The function ϕ has the Lagrange-like property $\phi(kh) = \delta_{0k}$ for $k = -m, \dots, m$ and is compactly supported such that $\phi(r) = 0$ for $|r| > hm$. An example of $\phi(r)$ for $n = 5$ ($m = 3$) is shown in Figure 3. If vectors $\boldsymbol{\phi}$ and \mathbf{u} are defined to be

$$\boldsymbol{\phi} = \begin{bmatrix} \phi_{1-m} \\ \phi_{2-m} \\ \vdots \\ \phi_{N+m-2} \\ \phi_{N+m-1} \end{bmatrix}, \quad \mathbf{u} = \begin{bmatrix} u_{1-m} \\ u_{2-m} \\ \vdots \\ u_{N+m-2} \\ u_{N+m-1} \end{bmatrix}, \quad (32)$$

then interpolant (30) can be rewritten as

$$\mathbf{u} = \boldsymbol{\phi}^T \mathbf{u}. \quad (33)$$

In the case of the extrapolated boundary treatment, only a subset of the grid points are actually stored/updated. Letting $\underline{\mathbf{u}}$ be this subset, then $\mathbf{u} = \mathbf{E}\underline{\mathbf{u}}$ where \mathbf{E} extrapolates the boundary points and copies the interior points.

In order to use the GD basis in the DG formulation, we need to be able to both compute integrals and derivatives of GD based approximations. Since over each subcell the GD approximation is polynomial, integrals can be simply computed by using quadrature over each subcell. Namely, let the N_q quadrature weights $\{\omega_k\}_{k=1}^{N_q}$ and points $\{\xi_k\}_{k=1}^{N_q}$ approximate integrals over $[-1, 1]$, then the inner product of $u, v \in W_{N,n}$ is

$$\begin{aligned} \int_{-1}^1 v(r)u(r) dr &= \sum_{i=0}^{N-1} \int_{r_i}^{r_{i+1}} v(r)u(r) dr = \sum_{i=0}^{N-1} \frac{1}{h} \int_{-1}^1 u\left(\frac{r_i + r_{i+1} + h\xi}{2}\right) v\left(\frac{r_i + r_{i+1} + h\xi}{2}\right) d\xi \\ &\approx \frac{1}{h} \sum_{i=0}^{N-1} \sum_{k=1}^{N_q} \omega_k v\left(\frac{r_i + r_{i+1} + h\xi_k}{2}\right) u\left(\frac{r_i + r_{i+1} + h\xi_k}{2}\right). \end{aligned} \quad (34)$$

In our case we use a $2m$ -point Legendre–Gauss quadrature rule, which integrates polynomials of degree $4m + 1$ exactly and thus the quadrature inner product is exact (since over each subcell the degree of uv is $2n = 4m - 2$). An example for $n = 5$ ($m = 3$) of the two grids (the GD grid and Legendre–Gauss) quadrature grid is shown in Figure 4. The inner product (34) can be written in matrix vector product form as

$$\int_{-1}^1 vu = \mathbf{v}^T \bar{\mathbf{L}}^T \bar{\mathbf{W}} \bar{\mathbf{L}} \mathbf{u} = \mathbf{v}^T \bar{\mathbf{M}} \mathbf{u}, \quad (35)$$

the overbar accent is used here to highlight that these are matrices for the one-dimensional basis functions. Here the diagonal matrix of composite quadrature weights is $\bar{W} = (\mathbf{I}_N \otimes \omega)/h$ with \otimes being the matrix Kronecker product, \mathbf{I}_N the $N \times N$ identity matrix, and ω the diagonal matrix of $\{\omega_k\}_{k=1}^{N_q}$. The Matrix \bar{L} is the interpolation matrix from GD grid points to the intra-subcell quadrature points. Regardless of the boundary closure, the mass matrix \bar{M} is banded with bandwidth $m + 1$.

In order to take derivatives of GD based solutions, we first note that even if $u \in W_{N,n}$ in general $u' \notin W_{N,n}$. That said, we can exploit the fact that over each subcell u is polynomial. Namely, in order to take derivatives we first interpolate the solution to the previous quadrature grid and then take derivatives discretely at the quadrature grid. Namely, we define the GD derivative matrix

$$\bar{D} = h(\mathbf{I}_N \otimes \mathbf{D}_q)\mathbf{L} \quad (36)$$

where \mathbf{D}_q is the polynomial derivative matrix for a function defined at the quadrature nodes $\{\zeta_k\}_{k=1}^{N_q}$; scaling by h arises because the quadrature nodes are for the interval $[-1, 1]$. We note that the stiffness matrix

$$\bar{S} = \bar{L}^T \bar{W} \bar{D} \quad (37)$$

will be exact as long as the quadrature rule used over the subcells is of order $2n - 1$. The stiffness matrix \bar{S} has the same banded structure as \bar{M} .

4.2. Two-Dimensional Galerkin Difference Operators

The one-dimensional GD basis and operators can be extended to multiple dimensions via the tensor product. Namely, let the two-dimensional domain $\hat{\Omega} = [-1, 1] \times [-1, 1]$ be discretized using $(N_r + 1) \times (N_s + 1)$ interior points, so that the grid points are $(r_i, s_j) = (ih_r - 1, jh_s - 1)$ with $h_r = 2/N_r$ and $h_s = 2/N_s$. Over each subcell $R_{ij} = [r_i, r_{i+1}] \times [s_j, s_{j+1}]$ an $n = 2m - 1$ degree tensor product polynomial is defined using nearby grid points. Namely, for $(r, s) \in R_{ij}$ the GD interpolation of u would be

$$u(r, s) = \sum_{j=1-m}^m \sum_{l=1-m}^m u_{i+j, j+l} l_j(r - ih_r) l_l(s - jh_s), \quad (38)$$

where l_k and l_l are the previously defined one-dimensional Lagrange polynomials and $u_{i,j}$ are the GD grid points values (see (29)); we say that a function in the form of (38) is in the space $W_{N_r \times N_s, n} = W_{N_r, n} \times W_{N_s, n}$. With this tensor product form, the approximation over each cell R_{ij} is constructed using a box of $(2m)^2$ grid points near the cell, grid points (r_{i+1-m}, r_{j+1-m}) through (r_{i+m}, s_{j+m}) . Using the previously defined GD basis functions ϕ_k , see (30) and (31), the approximation over the whole domain can be written as

$$u(r, s) = \sum_{i=1-m}^{N_r+m-1} \sum_{j=1-m}^{N_s+m-1} u_{i,j} \phi_i(r; h_r) \phi_j(s; h_s); \quad (39)$$

here the parameter h has been added to $\phi_i(r; h)$ since each dimension is allowed to have a different grid spacing. In two dimensions, the grid function is denoted with the vector

$$\mathbf{u} = \left[u_{-g, -g} \quad u_{-g, -g+1} \quad u_{-g, -g+2} \quad \cdots \quad u_{N_r+g, N_s+g} \right]^T. \quad (40)$$

With this, the interpolant can be written as

$$u(r, s) = (\boldsymbol{\phi}_s(s) \otimes \boldsymbol{\phi}_r(r))^T \mathbf{u}, \quad (41)$$

with \otimes being the matrix Kronecker product and $\boldsymbol{\phi}_r$ and $\boldsymbol{\phi}_s$ being the stacking of basis functions $\{\phi_k(r; h_r)\}_{k=1-m}^{N_r+m-1}$ and $\{\phi_k(r; h_s)\}_{k=1-m}^{N_s+m-1}$.

The two-dimensional operators needed to define the DG scheme over a GD element are then

$$\mathbf{W} = \bar{\mathbf{W}}_s \otimes \bar{\mathbf{W}}_r, \quad \mathbf{L} = \bar{\mathbf{L}}_s \otimes \bar{\mathbf{L}}_r, \quad (42)$$

$$\mathbf{D}_r = \bar{\mathbf{L}}_s \otimes \bar{\mathbf{D}}_r, \quad \mathbf{D}_s = \bar{\mathbf{D}}_s \otimes \bar{\mathbf{L}}_r, \quad (43)$$

where the subscripts r and s on the one-dimensional GD matrices indicate that these are define with respect to grids of size N_r and N_s , respectively.

The GD reference mass matrix is

$$\mathbf{M} = \mathbf{L}^T \mathbf{W} \mathbf{L} = (\bar{\mathbf{L}}_s^T \bar{\mathbf{W}}_s \bar{\mathbf{L}}_s) \otimes (\bar{\mathbf{L}}_r^T \bar{\mathbf{W}}_r \bar{\mathbf{L}}_r) = \bar{\mathbf{M}}_s \otimes \bar{\mathbf{M}}_r. \quad (44)$$

Since the reference mass matrix has a tensor product structure its inverse will as well:

$$\mathbf{M}^{-1} = \bar{\mathbf{M}}_s^{-1} \otimes \bar{\mathbf{M}}_r^{-1}. \quad (45)$$

This means that when \mathbf{M}^{-1} is applied, it can be done dimension-by-dimension using a banded Cholesky factorization of $\bar{\mathbf{M}}_s$ and $\bar{\mathbf{M}}_r$. Unfortunately, when the element is not affine the Jacobian determinant weighted mass matrix does not have this tensor product structure and the full factorization would be required to apply \mathbf{M}_J^{-1} , thus motivating the use of the weight-adjusted methodology.

4.3. Construction of Metric Terms

In the DG scheme (17)–(19) metric terms are required at the quadrature nodes. Of course one option is to store the metric terms (or their approximation) at the quadrature nodes. In the case of GD though, this greatly increases the storage since the ratio of quadrature nodes to GD grid points is $4m^2$ in two-dimensions (assuming that the basis of the one-dimensional quadrature is a $2m$ -point Legendre–Gauss quadrature rule). Thus, for a practical implementation of GD, we suggest storing the volume metric terms at the GD interpolation nodes and interpolating them on-the-fly to the quadrature nodes; of course another option, if the exact metric terms were available, would be to compute them on-the-fly at the quadrature nodes. The following construction, except where noted, holds for both GD and simplicial elements.

Let $x, y \in V_h^e$, we then define the metric derivatives as the L^2 -projection of the exact derivatives into the approximation space. For instance, we let the function $x_r \in V_h^e$ be such that

$$\int_{-1}^1 \int_{-1}^1 v \left(x_r - \frac{dx}{dr} \right) = 0 \quad (46)$$

for all $v \in V_h^e$; an analogous construction is used to define $x_s, y_r, y_s \in V_h^e$. In matrix-vector form all of the metric derivatives are then

$$\mathbf{x}_r = \mathbf{M}^{-1} \mathbf{L}^T \mathbf{W} \mathbf{D}_r \mathbf{x}, \quad \mathbf{x}_s = \mathbf{M}^{-1} \mathbf{L}^T \mathbf{W} \mathbf{D}_s \mathbf{x}, \quad (47)$$

$$\mathbf{y}_r = \mathbf{M}^{-1} \mathbf{L}^T \mathbf{W} \mathbf{D}_r \mathbf{y}, \quad \mathbf{y}_s = \mathbf{M}^{-1} \mathbf{L}^T \mathbf{W} \mathbf{D}_s \mathbf{y}. \quad (48)$$

For GD elements these reduce to

$$\mathbf{x}_r = \left(\mathbf{I}_{N_s} \otimes \left(\bar{\mathbf{M}}_r^{-1} \bar{\mathbf{L}}_r^T \bar{\mathbf{W}}_r \bar{\mathbf{D}}_r \right) \right) \mathbf{x}, \quad \mathbf{x}_s = \left(\bar{\mathbf{M}}_s^{-1} \bar{\mathbf{L}}_s^T \bar{\mathbf{W}}_s \bar{\mathbf{D}}_s \right) \otimes \left(\mathbf{I}_{N_r} \right) \mathbf{x}, \quad (49)$$

$$\mathbf{y}_r = \left(\mathbf{I}_{N_s} \otimes \left(\bar{\mathbf{M}}_r^{-1} \bar{\mathbf{L}}_r^T \bar{\mathbf{W}}_r \bar{\mathbf{D}}_r \right) \right) \mathbf{y}, \quad \mathbf{y}_s = \left(\bar{\mathbf{M}}_s^{-1} \bar{\mathbf{L}}_s^T \bar{\mathbf{W}}_s \bar{\mathbf{D}}_s \right) \otimes \left(\mathbf{I}_{N_r} \right) \mathbf{y}, \quad (50)$$

which means that for GD these calculations can be performed along the grid lines. We then define the metric terms needed at the quadrature nodes as the interpolation of these metric derivatives. Namely, we define

$$\mathbf{J} \mathbf{r}_x = \text{diag}(\mathbf{L} \mathbf{y}_s), \quad \mathbf{J} \mathbf{r}_y = \text{diag}(-\mathbf{L} \mathbf{x}_s), \quad \mathbf{J} \mathbf{s}_x = \text{diag}(-\mathbf{L} \mathbf{y}_r), \quad \mathbf{J} \mathbf{s}_y = \text{diag}(\mathbf{L} \mathbf{x}_r), \quad (51)$$

where the operator $\text{diag}(\cdot)$ turns a vector into a diagonal matrix. When needed, the Jacobian determinant can be computed from these interpolated values as:

$$\mathbf{J} = \left(\mathbf{J} \mathbf{r}_y \right) \left(\mathbf{J} \mathbf{s}_x \right) - \left(\mathbf{J} \mathbf{r}_x \right) \left(\mathbf{J} \mathbf{s}_y \right). \quad (52)$$

An important property of our approach to computing the metric terms is that we preserve discretely the divergence theorem, which will enable us to show that the scheme can be made both conservative and constant preserving.

Theorem 4.1. *An element with metric terms computed using (51) with (47)–(48) satisfies*

$$\mathbf{1}^T \mathbf{S}_x \mathbf{v}_x + \mathbf{1}^T \mathbf{S}_y \mathbf{v}_y = \int_{\partial e} S_J (n_x v_x + n_y v_y), \quad (53)$$

for all $v_x, v_y \in V_h^e$ where the surface Jacobian S_J and outward normal $[n_x \ n_y]^T$ are calculated using $x, y \in V_h^e$; here $\mathbf{1}$ is the vector of ones.

Proof. See Appendix Appendix B □

Theorem 4.1 alone is not enough to guarantee a conservative and constant preserving scheme. In concert with Theorem 4.1 we need the following consistency statement about the mortar and element surface integrals:

$$\int_{\partial e} S_J (n_x v_x + n_y v_y) = \sum_{g \in \mathcal{G}^e} \mathbf{1}^T (\mathbf{L}^g)^T \mathbf{S}_J^g \mathbf{W}^g \mathbf{v}_n^-, \quad (54)$$

for all $v_x, v_y \in V_h^e$. With this we now have the following result concerning the conservation and constant preserving properties of the scheme.

Theorem 4.2. *If all of the elements $e \in \mathcal{E}$ satisfy both Theorem 4.1 and (54), then scheme (17)–(19) is both conservative and constant preserving with periodic boundary conditions.*

Proof. See Appendix Appendix C □

For the two-dimensional problems considered here, the assumption of (54) holds if:

1. the surface Jacobian determinant times the components of the unit normal on g is $S_J^g n_x^-, S_J^g n_y^- \in \mathbb{P}_n$ (e.g., a polynomial in the mortar space);
2. the quadrature on the mortar can integrate polynomials of degree $2n$, (e.g., the right-hand side of (54) is exact); and
3. on both sides of each mortar element g , the physical coordinates are discretely conforming, e.g., $x^- = x^+$ and $y^- = y^+$ along the interface.

The implications of point 3 for GD elements comes from the fact that the only function that is in both $W_{N_1, n}$ and $W_{N_2, n}$ for $N_1 \neq N_2$ are functions in \mathbb{P}_n . Thus, along nonconforming GD interfaces, the coordinate transform must be a single polynomial along the entire interface. For purely computational interfaces, this is not much of a limitation (since interfaces between elements are artificial). For problems with physical interfaces, such as a layered discontinuous materials (not considered here), resolving the geometry more accurately requires increasing the number of elements along the interface not (only) increasing the number of grid points inside the elements. Of course, these are only considerations if conservation and constant preserving properties are needed. Additionally, when GD elements are coupled with simplicial elements this is likely not a constraint, since the GD elements would likely be affine with any complexity in the geometry handled using the more flexible curved simplicial elements.

For three-dimensional problems, more restrictions on the geometry are needed to insure the conservation and constant preserving properties. Namely, in both the conforming and nonconforming cases care is needed to insure that certain metric products are in the approximation space; see for instance [14] for the conforming case and [11] for the nonconforming case.

5. Results

In this section we test the properties of the above defined discretization. The tests are broken into two sets. We begin by testing the weight-adjusted discontinuous Galerkin method (WADG) with the GD basis. We test the accuracy of the WADG projection for the GD basis and then test the constant-preserving, conservation, and accuracy properties of the scheme on nonconforming curved GD meshes. We then move on to the coupling of GD elements with simplicial elements, first comparing the time step restrictions of each of the methods and then moving on to the accuracy of the

coupled scheme; in all the coupled test problems the GD order and polynomial order used on simplicial elements are chosen to be the same.

In all tests, the Taylor time integration is used to advance the semidiscrete scheme. Namely, in all cases the semidiscrete scheme can be written as

$$\frac{d\mathbf{w}}{dt} = \mathbf{A}\mathbf{w}, \quad (55)$$

with \mathbf{w} being the solution vector and \mathbf{A} being the spatial discretization. The k^{th} order accurate Taylor time stepping scheme is

$$\mathbf{w}(t + \Delta t) \approx \sum_{l=0}^k \frac{\Delta t^l}{l!} \mathbf{A}^l \mathbf{w}(t), \quad (56)$$

where Δt is the time step size. The scheme is locally stable (e.g., the stability region crosses the imaginary axis) for orders $k = 4l - 1$ and $k = 4l$ with $l \in \mathbb{Z}^+$. The temporal order k used is the minimum local stable k such that $k > n$, e.g., the temporal order both locally stable and at least one order higher than the spatial order.

Throughout, error in the solution is measured using the energy norm

$$\text{error} = \sqrt{\frac{1}{2} \sum_{e \in \mathcal{E}} \int_e J (\Delta p^2 + \Delta v_x^2 + \Delta v_y^2)}, \quad (57)$$

where Δp , Δv_x , and Δv_y are the difference between the computed and exact solutions. The integrals in (57) are approximated using the element quadrature rule, with differences between the computed and exact solutions evaluated at the quadrature points. Results are reported with respect to refinement level. For GD elements refinement is done with grid doubling (e.g., the 1-D grid spacing is cut in half with each level of refinement). For the simplicial elements refinement is done by quadrisection (e.g., each reference triangle is split into four similar triangles).

The codes used in this paper are freely available at <https://github.com/bfam/GDComplexGeometries>. The simplicial element scheme is implemented using MATLAB codes from [13].

5.1. WADG-GD Projection Accuracy

We begin by testing the accuracy of the weight-adjusted approximation for GD elements as well as the storage of the metric terms at the GD interpolation nodes. Namely, we want to quantify the error made in the approximation of the L^2 -projection of a function $f(x, y)$ into the curved-GD approximation space. Following [15], we consider the coordinate transform

$$x = r + \beta \cos\left(\frac{3\pi s}{2}\right) \cos\left(\frac{\pi r}{2}\right), \quad y = s + \beta \sin\left(\frac{3\pi r}{2}\right) \cos\left(\frac{\pi s}{2}\right). \quad (58)$$

Here the domain is $-1 \leq r, s \leq 1$ and β is a parameter which controls the regularity of the transform. We let there be a single GD element with an interior grid of $(N + 1) \times (N + 1)$ points, e.g., the GD grid spacing is $h = 2/N$ in each dimension.

The L^2 -projection of a function $f(x, y)$ into the GD approximation space is defined to be the function $\bar{f} \in V_h$ such that

$$\int_{\hat{\Omega}} \phi J (f - \bar{f}) = 0, \quad \forall \phi \in V_h. \quad (59)$$

Here $V_h = W_{N \times N, n}$ and the Jacobian determinant is J . Using GD quadrature to approximate the integrals gives the matrix problem:

$$\mathbf{M}_J \bar{\mathbf{f}} = \mathbf{L}^T \mathbf{W} \mathbf{f}_q, \quad (60)$$

where \mathbf{f}_q is the exact f evaluated at the quadrature nodes and $\tilde{\mathbf{f}}$ is the projection of f into the GD space. We define the L^2 -error in the approximation as

$$e_{L2} = \int_{\Omega} J(f - \tilde{f})^2 \approx \Delta_q^T \mathbf{W} \mathbf{J} \Delta_q, \quad \Delta_q = \mathbf{f}_q - \mathbf{L} \tilde{\mathbf{f}}. \quad (61)$$

The error e_{L2} depends on f , the mesh skewness parameter β , the number of points N , the GD approximation order n , the boundary treatment, and any approximations used for \mathbf{M}_J . Three different approaches to handling \mathbf{M}_J will be considering:

- L^2 -projection: the mass matrix $\mathbf{M}_J = \mathbf{L}^T \mathbf{W} \mathbf{J} \mathbf{L}$ with the exact Jacobian determinant evaluated at the quadrature points;
- WAGD: weight-adjusted approximation of the mass matrix with $\mathbf{M}_{1/J} = \mathbf{L}^T \mathbf{W} \mathbf{J}^{-1} \mathbf{L}$ evaluated using the exact Jacobian determinant evaluated at the quadrature points; and
- inexact WAGD: weight-adjusted approximation of the mass matrix with $\mathbf{M}_{1/J}$ evaluated using \mathbf{J} as defined by (52) with the coordinate points x and y projected into the GD space using the same quadrature rule, e.g., $\mathbf{M} \tilde{\mathbf{x}} = \mathbf{L}^T \mathbf{W} \mathbf{x}$ with \mathbf{x} being x evaluated at the quadrature nodes and \mathbf{M} being the reference GD mass matrix.

In all cases the exact Jacobian determinant is used when evaluating the right-hand side of (60) and in the computation of the error (61). For all tests, the base mesh uses $n = N$.

Figures 5 and 6 show the results for $\beta = 1/8$ and $\beta = 0.22$, respectively, using both the extrapolation (top row) and ghost basis (bottom row) method with polynomial order $n = 5$. The function being approximated in both cases is $f(x, y) = \cos(kx) \cos(ky)$ with $k = \pi/2$ (left column) and $k = 5\pi$ (right column); here the lower the value of k the smoother the function and the better the overall approximation will be. In the figures the L^2 -error for the L^2 -projection, WADG, and inexact WADG are all plotted, but are not visible as they lie on top of one another. Therefore we also show the difference between WAGD and the L^2 -projection (labeled *delta WADG*) as well as the difference between inexact WAGD and the L^2 -projection (labeled *delta inexact WADG*).

As can be seen both WADG and inexact WADG are accurate, and in most cases the error is on the same order as the L^2 -projection; this is indicated by the fact that the delta lines are below the L^2 -projection lines. In all cases the weight-adjusted approaches are high-order accurate and storing the metric terms at the GD interpolation nodes does not significantly impact the accuracy of the weight-adjusted approach. As the theory of [12] suggests, the weight-adjusted approaches does better with more regular geometry mappings (lower β values), which explains the fact that at lower resolutions the delta lines are above the L^2 -projection curves for $k = \pi/2$ and $\beta = 0.22$. In all the tests the ghost basis method outperforms the extrapolation method for the same grid spacing, though it is worth noting that for the same grid spacing the ghost basis method has $\sim 4(n-1)N$ more degrees of freedom than the extrapolation method.

Though not shown, we note that with $n = 3$ and $\beta = 0.22$ the approximated Jacobian determinant had a negative value when $N = 6$, which shows that storage of the Jacobian determinant at the interpolation nodes requires that the geometry approximation be sufficiently well-resolved for this storage strategy to work in practice.

One approach that could be used if under-resolved geometries were needed would be to store the square root of the Jacobian determinant at the GD interpolation nodes. Namely, first the square root of the Jacobian determinant is computed at the GD quadrature nodes:

$$\tilde{\mathbf{J}}_{sq} = \sqrt{(\mathbf{D}_r \mathbf{x}) \odot (\mathbf{D}_s \mathbf{y}) - (\mathbf{D}_s \mathbf{y}) \odot (\mathbf{D}_r \mathbf{y})}, \quad (62)$$

where \odot is the Hadamard (componentwise) product of two vectors and the square root is applied componentwise. The square root of the Jacobian determinant at the quadrature nodes $\tilde{\mathbf{J}}_{sq}$ is then projected to the GD interpolation nodes for storage:

$$\mathbf{J}_{sq} = \mathbf{M}^{-1} \mathbf{L}^T \mathbf{W} \tilde{\mathbf{J}}_{sq}. \quad (63)$$

When the Jacobian determinant is needed at the quadrature nodes the square root of the Jacobian determinant is interpolated and squared:

$$\mathbf{J} = (\mathbf{L} \mathbf{J}_{sq})^2, \quad (64)$$

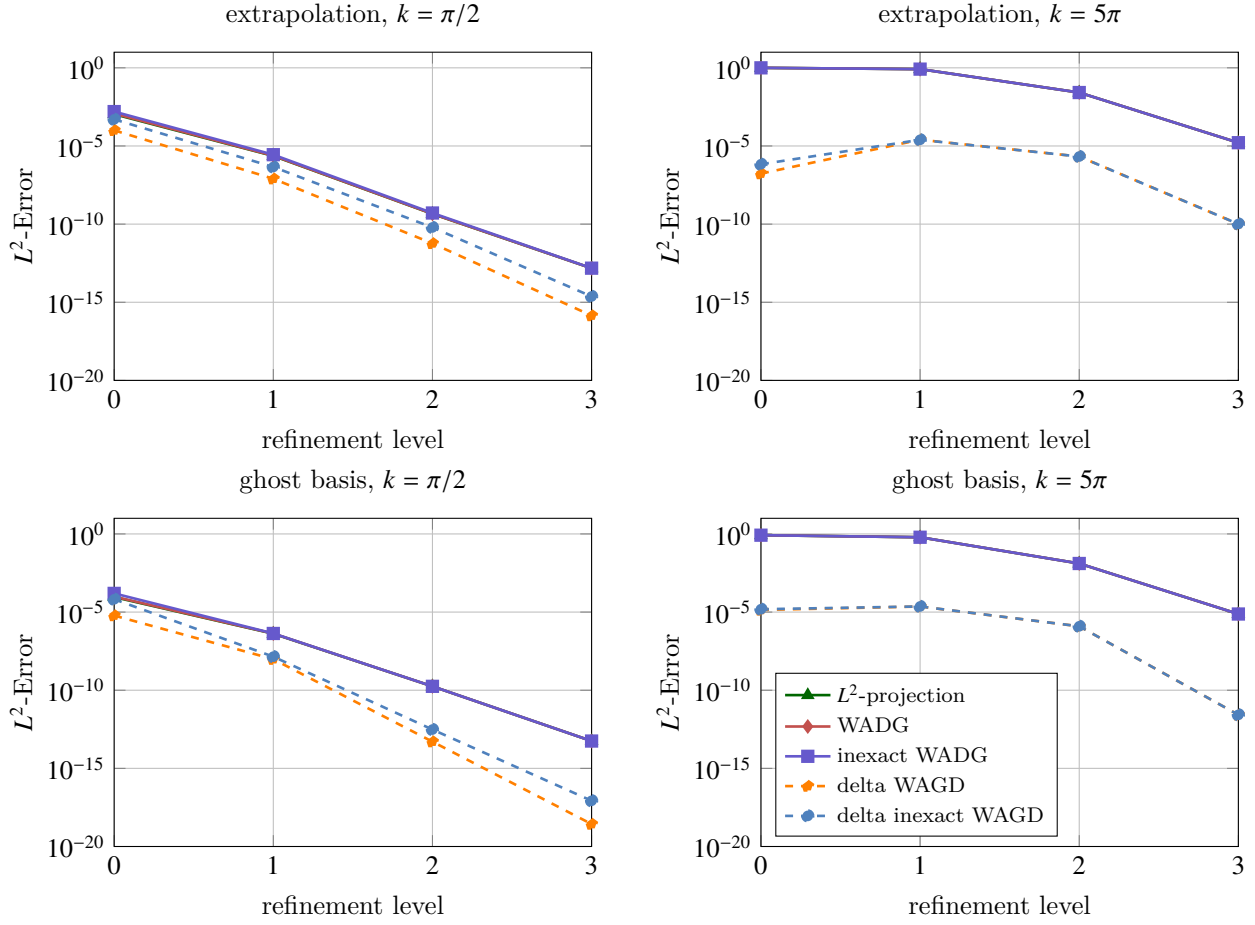


Figure 5: Error in representing $f(x, y) = \cos(kx) \cos(ky)$ with a GD approximation ($n = 5$) on a grid defined by (58) with $\beta = 1/8$. The base mesh used $(n + 1) \times (n + 1)$ interior GD nodes.

where the square is applied componentwise; the form of (64) is a replacement for (52) which is the computation of the Jacobian determinant from the metric derivatives after they have been interpolated to the quadrature nodes. Tests (not shown) have verified that this approach seems to have minimal impact on the accuracy of the scheme when the solution is well-resolved.

5.2. Constant Preservation, Conservation, and Energy Stability of WADG-GD

Here we examine the constant-preserving and conservation properties of WADG-GD with the computation of metric terms given in Section 4.3. In this test we consider the domain defined by the transformation

$$x = r \cos(\beta) + s \sin(\beta), \quad y = -r \sin(\beta) + s \cos(\beta), \quad \beta = \frac{\pi}{4} (1 - r^2)(1 - s^2). \quad (65)$$

Here the domain is $-1 \leq r, s \leq 1$. The domain is discretized using four GD elements as shown in Figure 7 using 16×16 (interior) GD mesh in the bottom-right and top-left elements and a 21×21 (interior) GD mesh for the other two elements.

We consider two approaches to handling the geometry. In the first case we project the transformation (65) into the GD space; the L^2 -projection is approximated using the GD quadrature grid. Across non-conforming interfaces the mesh will be discretely discontinuous because the elements on either side of the interface have different representations of the geometry. This means that the mortar element based metric terms will be different than (at least one of) the GD element metric terms; in our case we calculate metric terms on the mortar by averaging x and y values from the two

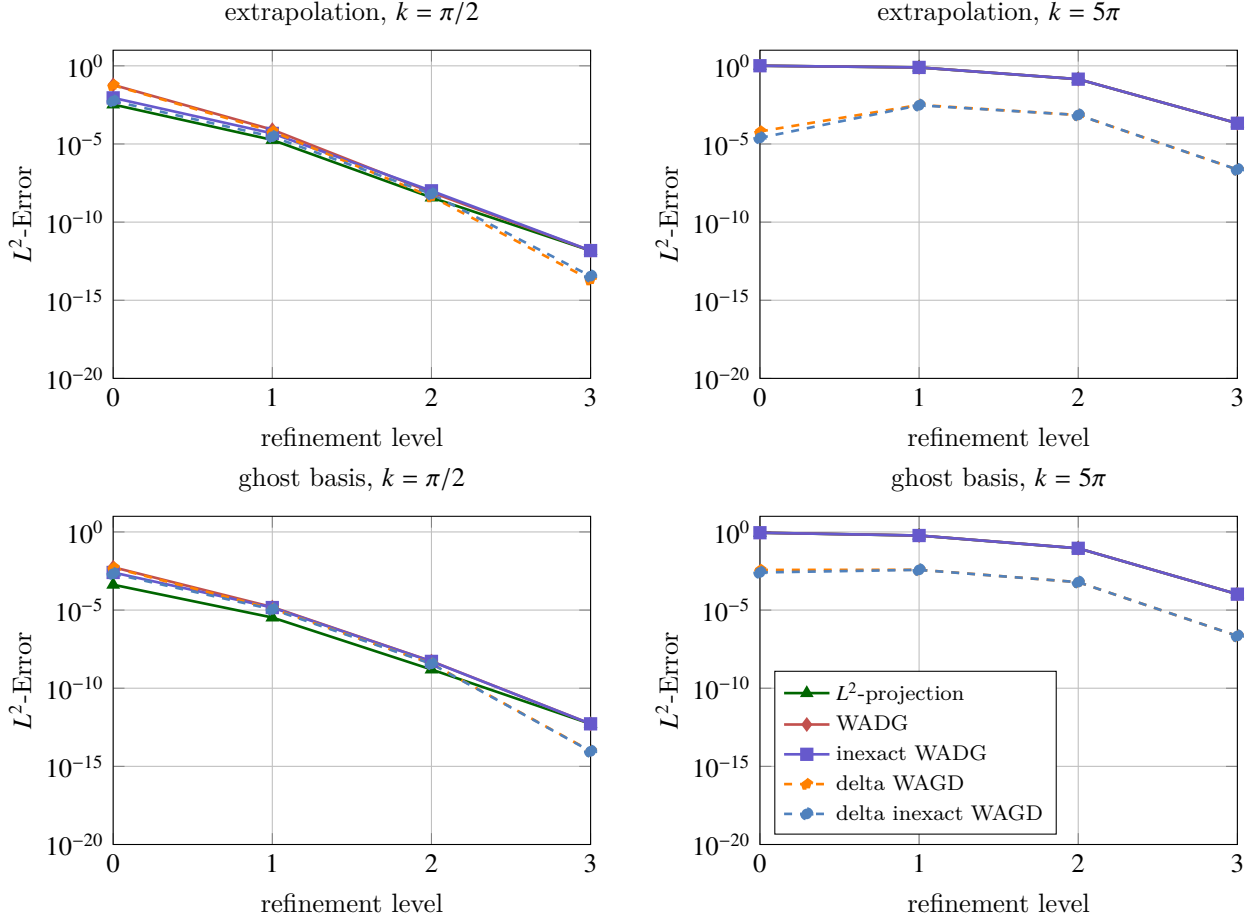


Figure 6: Error in representing $f(x, y) = \cos(kx) \cos(ky)$ with a GD approximation ($n = 5$) on a grid defined by (58) with $\beta = 0.22$. The base mesh used $(n + 1) \times (n + 1)$ interior GD nodes.

sides of each mortar element at the mortar element quadrature nodes. We call this first approach the *discontinuous geometry approximation*. Note that even if the mesh is conforming, the L^2 -projection can cause the geometry to be discretely discontinuous if continuity is not enforced between elements.

In the second case, the mesh is made watertight by modifying the x and y values at the GD interpolation nodes along the non-conforming interfaces. Namely, the grid values along the interface are replaced with values in \mathbb{P}_n . These values are calculated along each interface using an L^2 -projection which preserves corner values. For instance, the points along the interface $-1 \leq r \leq 1$ and $s = -1$ are $\bar{x}, \bar{y} \in \mathbb{P}_n$ which satisfy for all $\phi \in \mathbb{P}_n$:

$$\int_{-1}^0 \phi(r)(x(r, -1) - \bar{x}(r)) = 0, \quad \bar{x}(-1) = x(-1, -1), \quad \bar{x}(0) = x(0, -1), \quad (66)$$

$$\int_{-1}^0 \phi(r)(y(r, -1) - \bar{y}(r)) = 0, \quad \bar{y}(-1) = y(-1, -1), \quad \bar{y}(0) = y(0, -1). \quad (67)$$

Note that values at nodes not on the interface are not modified by this procedure. On both sides of the interface the projections are approximated using 21 Chebyshev nodes of the second kind, and thus both sides of the mortar elements use the same polynomial along the interface. Since the coordinate points on the interface are the same for both sides of the element, constraint (54) is satisfied and Theorem 4.2 applies. We call this second approach the *watertight geometry approximation*.

In order to test the ability of the scheme to preserve constants, we use the initial condition $v_x = 1, v_y = 2$,

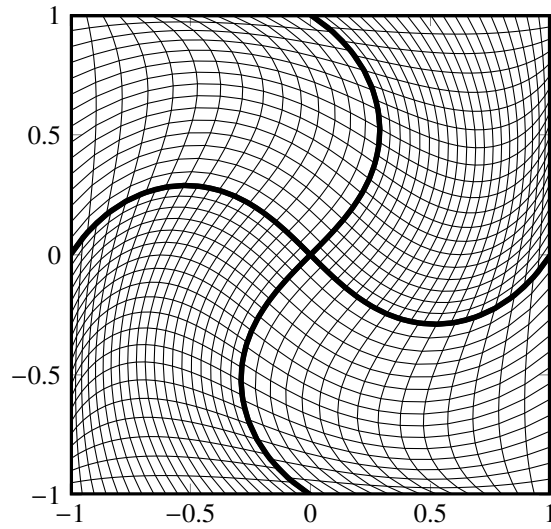


Figure 7: Skewed mesh used for the constant preservation and conservation test problem defined by global transformation (65).

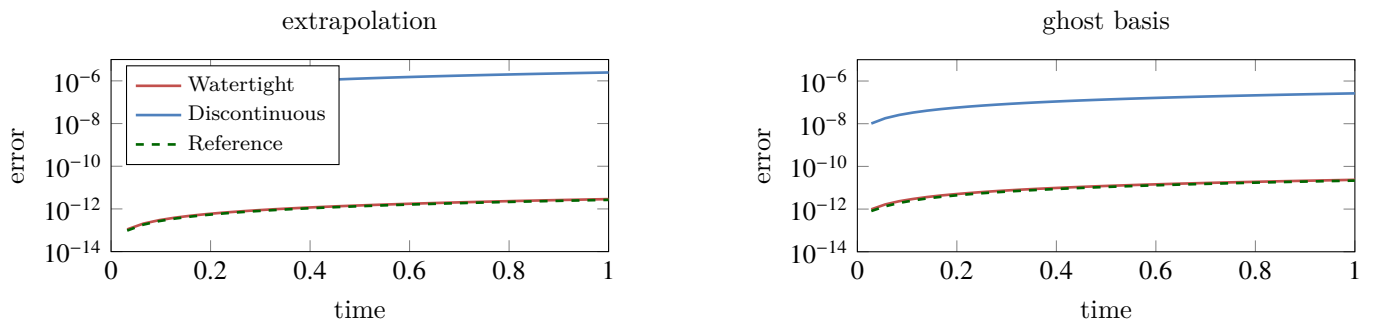


Figure 8: Error versus time for the constant preservation test using mesh given in Figure 7 with $n = 7$.

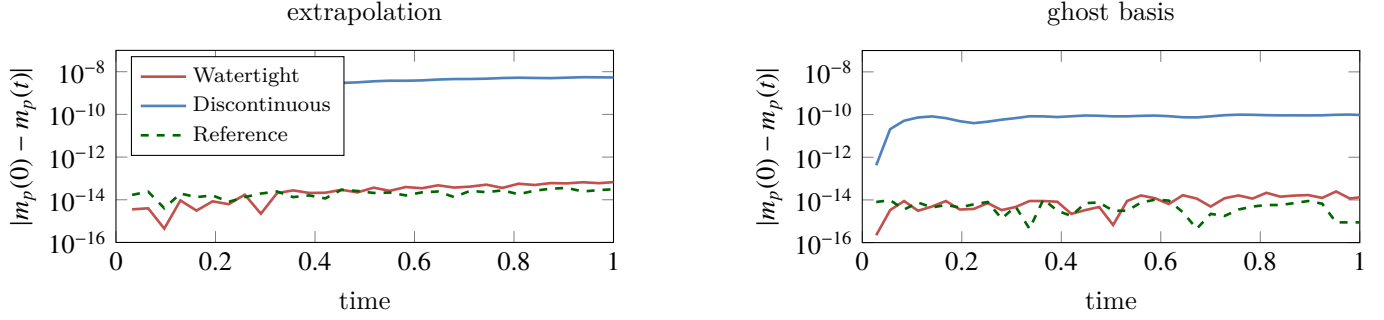


Figure 9: Change in m_p versus time for the conservation test using mesh given in Figure 7 with $n = 7$.

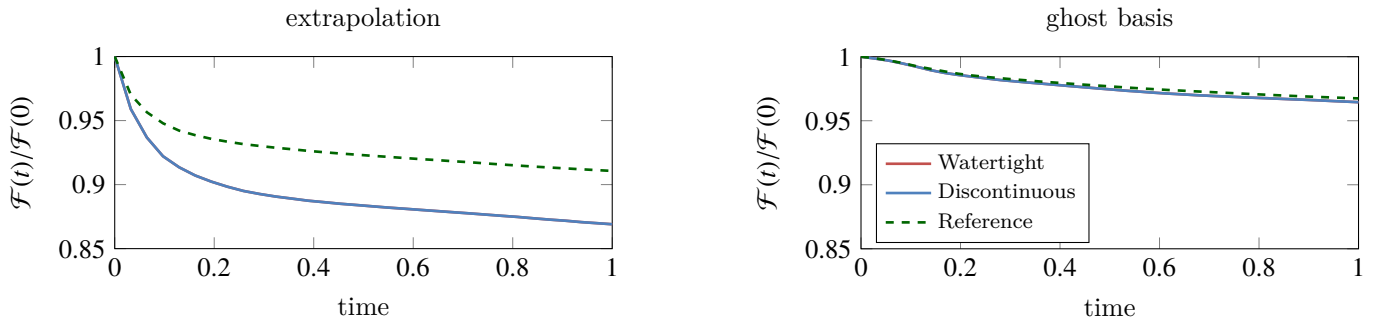


Figure 10: Normalized energy versus time using a pseudorandom initial condition with mesh given in Figure 7 for $n = 7$.

and $p = 3$ with periodic boundary conditions. If the scheme preserved constants the initial values will not change with time, in other words the error in the solution should be (approximately) zero. In Figure 8 the error for both the watertight and discontinuous geometry approximations are shown for both the extrapolation and ghost basis GD methods with $n = 7$. Also included in the figure the results from a conforming reference mesh. In the conforming reference case each GD element is discretized using a 21×21 (interior) GD mesh; note that since the L^2 -projection of the coordinate transformation is done element by element the geometry will be discontinuous, thus to make the geometry watertight in the conforming case we interpolate the transformation along the boundaries of the elements. As can be seen, the discontinuous geometry approximation has error growth with time whereas the watertight mesh matches the conforming reference case.

In order to test the conservation properties of the scheme, we use a pseudorandom initial condition with periodic boundary conditions. We then define the mass in each component of the solution at time t to be

$$m_{v_x} = \mathbf{1}^T \mathbf{M} \mathbf{M}_{1/J}^{-1} \mathbf{M} \mathbf{v}_x, \quad m_{v_y} = \mathbf{1}^T \mathbf{M} \mathbf{M}_{1/J}^{-1} \mathbf{M} \mathbf{v}_y, \quad m_p = \mathbf{1}^T \mathbf{M} \mathbf{M}_{1/J}^{-1} \mathbf{M} \mathbf{p}. \quad (68)$$

We highlight that here we are not using \mathbf{M}_J but the WADG-GD mass matrix because it is with respect to this matrix that the scheme is conservative. In Figure 9 the absolute difference $|m_p(t) - m_p(0)|$ is given for $n = 7$ for the extrapolation and ghost basis GD methods; mass components m_{v_x} and m_{v_y} are conserved even in the discontinuous geometry case due to the use of the weak derivative (see Appendix Appendix C). As can be seen the discontinuous geometry is not conservative, whereas the watertight mesh has the same conservation properties as the conforming reference mesh.

We now turn to confirming the energy stability properties of the scheme. To do this, we use the pseudorandom initial condition with periodic boundary conditions. In Figure 10 normalized energy in the solution versus time is shown for $n = 7$ for both the extrapolation and ghost basis GD methods. As can be seen, both the schemes with all of the different geometry treatments dissipate energy in time as predicted by the previous stability analysis and the dissipation is essentially the same for both approximate geometry treatments; by using a pseudorandom initial value we are ensuring that energy is widely spread across the eigenmodes of the operator.

It is worth noting that the approach we have taken to make the mesh watertight will not work in general for

GD elements for several reasons. First, as the mesh within an element is refined the geometry approximation does not change. For homogeneous materials, as considered here, this is not a problem because the interface is purely computational (e.g., the accuracy of the solution does not depend on this interface being represented accurately). For heterogeneous materials with discontinuous material properties (not considered here) this may be a problem since convergence will require accurate resolution of the interface. An additional problem with this approach is that by only moving points on the interface it is possible that points will be moved past their neighbors, giving rise to a negative Jacobian determinant; this is in particular an issue at high resolution. Lastly, the modification of the geometry can result in a significant change in the time step restriction. For instance, when this problem was run with $n = 5$ the time step restriction for the watertight mesh was 6 times smaller than for the discontinuous mesh.

There are several possible approaches to address these issues if the constant-preserving and conservation properties are desired. For purely computational interfaces, a transfinite blending of the surface into the volume could be used instead of a global transform. This would mean that as the GD mesh is refined the element could not become inverted (assuming the transfinite blend did not invert the element). For physical interfaces, one could resolve the interface more accurately by adding elements to the mesh (as opposed to increasing the grid lines within the elements).

5.3. Accuracy of WADG-GD on Nonconforming Meshes

In this test, we explore the accuracy of WAGD-DG. Using the previously defined transform (65) (see Figure 9) and with the zero velocity boundary condition (2). For any $k \in \mathbb{Z}$ the modal solution

$$p = \sqrt{2} \cos\left(\pi k \frac{x+1}{2}\right) \cos\left(\pi k \frac{y+1}{2}\right) \cos\left(\frac{\sqrt{2}}{2} \pi k t\right), \quad (69)$$

$$v_x = \sin\left(\pi k \frac{x+1}{2}\right) \cos\left(\pi k \frac{y+1}{2}\right) \sin\left(\frac{\sqrt{2}}{2} \pi k t\right), \quad (70)$$

$$v_y = \cos\left(\pi k \frac{x+1}{2}\right) \sin\left(\pi k \frac{y+1}{2}\right) \sin\left(\frac{\sqrt{2}}{2} \pi k t\right), \quad (71)$$

satisfies governing equations (1) with (2) on $\Omega = [-1, 1] \times [-1, 1]$. Using $k = 15$ we run this test for both the extrapolation and ghost basis GD schemes with varying orders and mesh resolutions. The final time for the simulation is $t = 2\sqrt{2}/k$ which corresponds to one full oscillation of the solution. The base mesh for all orders is as shown in the figure; the bottom-right and top-left elements use an 16×16 (interior) GD mesh and a 21×21 (interior) GD mesh for the other two elements. We refine the mesh by doubling the resolution inside each element. For this test we only consider the discontinuous geometry representation, with an (approximate) L^2 -projection of the coordinate transform into the GD space.

Results for the test are shown in Figure 11 and Table 1. As can be seen, the method is converging at a high-order rate for each n as the resolution is increased. For the same grid spacing, the ghost basis method outperforms the extrapolation method.

5.4. Simplicial elements vs GD elements comparison

We now turn to the coupling of simplicial and GD elements. In order to motivate this coupling, in this section we seek to compare the time step restrictions and number of degrees of freedom needed for the two classes of schemes. The challenge in doing this is the selection of the mesh resolution for each method. Just choosing the two meshes so that they have the same number of degrees of freedom may not be the right choice, since even though the methods may converge at the same rate the constant multiplying the error terms may be different. We address this by setting the resolutions for each method so that the error for each method is roughly the same for a modal problem and then determine the maximum stable time step for each method. In this test, the simplicial mesh is taken to be a mesh of 64 right triangles; the mesh is generated by initially splitting the square into 4 right triangles and then iterative refining the mesh 2 times with quadrisection refinement.

In this test we take the domain to be the unit square $\Omega = [-1, 1] \times [-1, 1]$ with the modal solution (69). The mode number k_n used for each polynomial order n is given in Table 2. The mode number is selected to be the largest value k_n that results in an error smaller than 10^{-3} at time $t = 2\sqrt{2}/k_n$ using simplicial elements with polynomial order n ; as noted above the simplicial element mesh is fixed at 64 elements.

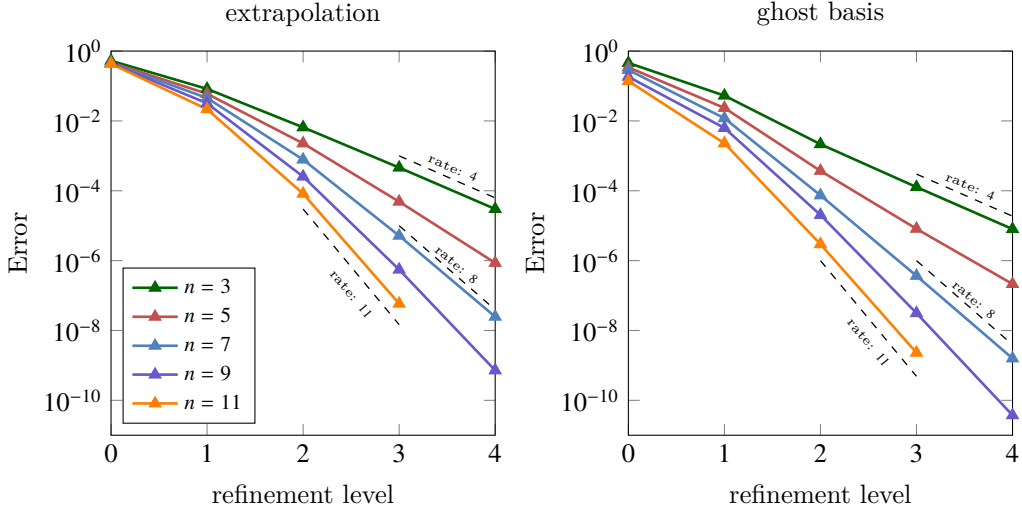


Figure 11: Error plot for extrapolation and ghost basis WADG-GD with modal solution (69) using coordinate transform (65).

level	$n = 3$ error (rate)	$n = 5$ error (rate)	$n = 7$ error (rate)	$n = 9$ error (rate)	$n = 11$ error (rate)
WADG-GD (extrapolation)					
0	5.28×10^{-1}	4.68×10^{-1}	4.50×10^{-1}	4.44×10^{-1}	4.31×10^{-1}
1	8.27×10^{-2} (2.67)	6.00×10^{-2} (2.96)	4.53×10^{-2} (3.31)	3.19×10^{-2} (3.80)	2.16×10^{-2} (4.32)
2	6.55×10^{-3} (3.66)	2.27×10^{-3} (4.72)	7.80×10^{-4} (5.86)	2.54×10^{-4} (6.97)	8.22×10^{-5} (8.04)
3	4.60×10^{-4} (3.83)	4.87×10^{-5} (5.54)	5.16×10^{-6} (7.24)	5.52×10^{-7} (8.85)	5.85×10^{-8} (10.46)
4	3.01×10^{-5} (3.94)	8.58×10^{-7} (5.83)	2.47×10^{-8} (7.71)	7.20×10^{-10} (9.58)	
WADG-GD (ghost basis)					
0	4.57×10^{-1}	3.42×10^{-1}	2.88×10^{-1}	1.83×10^{-1}	1.39×10^{-1}
1	5.30×10^{-2} (3.11)	2.35×10^{-2} (3.86)	1.19×10^{-2} (4.59)	6.28×10^{-3} (4.87)	2.29×10^{-3} (5.92)
2	2.16×10^{-3} (4.62)	3.71×10^{-4} (5.99)	7.39×10^{-5} (7.34)	2.03×10^{-5} (8.27)	2.95×10^{-6} (9.60)
3	1.27×10^{-4} (4.08)	8.14×10^{-6} (5.51)	3.66×10^{-7} (7.66)	3.13×10^{-8} (9.34)	2.30×10^{-9} (10.33)
4	7.99×10^{-6} (4.00)	2.14×10^{-7} (5.25)	1.59×10^{-9} (7.85)	3.74×10^{-11} (9.71)	

Table 1: Error and calculated rates for WADG-GD with modal solution (69) using coordinate transform (65).

n	k_n	extrapolation				ghost basis			
		N^E	$\frac{N_p^{\mathbb{P}}}{N_p^E}$	$\frac{\Delta t^E}{\Delta t^{\mathbb{P}}}$	$\frac{\Delta t^E N_p^{\mathbb{P}}}{N_p^E \Delta t^{\mathbb{P}}}$	N^G	$\frac{N_p^{\mathbb{P}}}{N_p^G}$	$\frac{\Delta t^G}{\Delta t^{\mathbb{P}}}$	$\frac{\Delta t^G N_p^{\mathbb{P}}}{N_p^G \Delta t^{\mathbb{P}}}$
3	1	15	2.5	2.2	5.6	11	3.3	1.7	5.4
5	4	27	1.7	1.7	2.9	24	1.6	1.3	2.1
7	7	30	2.4	1.9	4.6	23	2.6	1.4	3.5
9	12	38	2.3	1.8	4.3	30	2.3	1.3	3.1
11	15	43	2.6	1.9	4.9	34	2.5	1.6	3.9

Table 2: Polynomial discontinuous Galerkin and Galerkin Difference time step comparison

n	simplicial	extrapolation	ghost basis	m	ρ
	$\frac{n\Delta t^{\mathbb{P}}}{2r^{\mathbb{P}}}$	$\frac{\Delta t^E}{h^E}$	$\frac{\Delta t^G}{h^G}$		
3	0.31	0.51	0.28	4	-2.79
5	0.38	0.52	0.36	7	-3.95
7	0.36	0.44	0.24	8	-4.31
9	0.40	0.45	0.26	11	-5.45
11	0.38	0.41	0.27	12	-5.82

Table 3: CFL restriction comparison for simplicial and GD elements; see also Table 2. Here m is the order of the Taylor time stepping method that has been used and ρ minimum extent of the stability region.

For the GD method, the unit square is discretized using a single GD block that has $(N + 1) \times (N + 1)$ interior GD points; the total number of points depends on whether the extrapolation or ghost basis method is used. For each polynomial order n , the value of N is chosen to be the smallest value so that the error at time $t = 2\sqrt{2}/k_n$ is less than the simplicial element solution with the same polynomial order. Table 2 gives the value of N used for GD with the extrapolation and ghost basis boundary treatments; in the table superscript E is used for values related to the extrapolation GD method, subscript G is used for the ghost basis GD method, and \mathbb{P} for simplicial elements.

A first observation is that for the same grid spacing the ghost basis method is more accurate than the extrapolation method, namely $2/N^G > 2/N^E$. That said, in some cases ($n = 5$ and $n = 11$) the ghost basis method requires more degrees of freedom; for a given grid size the total degrees of freedom for the extrapolation method is $N_p^E = (N^E + 1)^2$ as compared with $N_p^G = (N^G + n)^2$ for the ghost basis method. That said, both GD element types outperform simplicial elements in terms of number of degrees of freedom; the 64 simplicial element mesh requires $N_p^{\mathbb{P}} = 64(n + 1)(n + 2)/2$ degrees of freedom. This is seen columns labeled $N_p^{\mathbb{P}}/N_p^E$ and $N_p^{\mathbb{P}}/N_p^G$ of Table 2 where the ratio total degrees of freedom is given. Since all these ratios are greater than 1, both GD element types are outperforming the simplicial elements with these parameters. This comparison is important because if the schemes are assumed to be memory bandwidth limited on current computing architectures, the total number of degrees of freedom can be taken as a proxy for the time to perform a single right-hand side evaluation.

We now turn to the consideration of the maximum stable time step for each method. We determine the maximum time step by initializing the solution vectors to pseudorandom values, then taking 100 time steps. The maximum time step is then the largest time step that results in no energy growth; by using a pseudorandom initial condition energy is spread across the eigenmodes of the numerical scheme. Table 2 gives the ratio of the maximum time step of the two GD methods (Δt^E and Δt^G) to the simplicial element method ($\Delta t^{\mathbb{P}}$); note that when comparing time steps the GD time step is on top and when comparing number of degrees of freedom DG was on top, thus in both cases numbers larger than 1 favor GD. As can be seen, for the given mesh resolutions, meshes with either of the GD element types can take larger time steps than meshes with simplicial elements. We also note that even though the ghost basis has more favorable accuracy for a given grid spacing, the time step is smaller.

An important observation for the time step restriction is that the ratio is roughly constant across polynomial orders once the error level for the schemes has been fixed. To explore this further, in Table 3 we give the CFL restrictions for each of the methods and polynomial orders. For simplicial elements, the time step is expected to scale with $2r^{\mathbb{P}}/n$ where $r^{\mathbb{P}}$ is the radius of the inscribe circle for the elements; on this mesh $r^{\mathbb{P}} = \sqrt{2}/4(1 + \sqrt{2})$. For the GD elements the time step should scale with mesh size, namely $h^E = 2/N^E$ and $h^G = 2/N^G$. As can be seen in Table 3, the time step restriction for the Taylor time integration method is roughly constant with respect to polynomial order for all three element types, and the extrapolation GD is favorable to the ghost basis GD by a factor of 1.5 to 2. We note that the stability region increases with order for the Taylor time integration method, so the extent of the eigenvalue spectra do increase with order. This can be seen in the last two columns of Table 3 where order of the Taylor time integration method for spatial order n and the minimum real extent of the stability region (ρ) is given.

To explore this further, Figure 12 shows the time step scaled eigenvalue spectra for the three methods with $n = 7$ along with the order 8 Taylor time integration scheme stability region; the eigenvalues and stability region have been computed numerically. As can be seen, it is a purely real eigenvalue that limits the time step for each method. For the

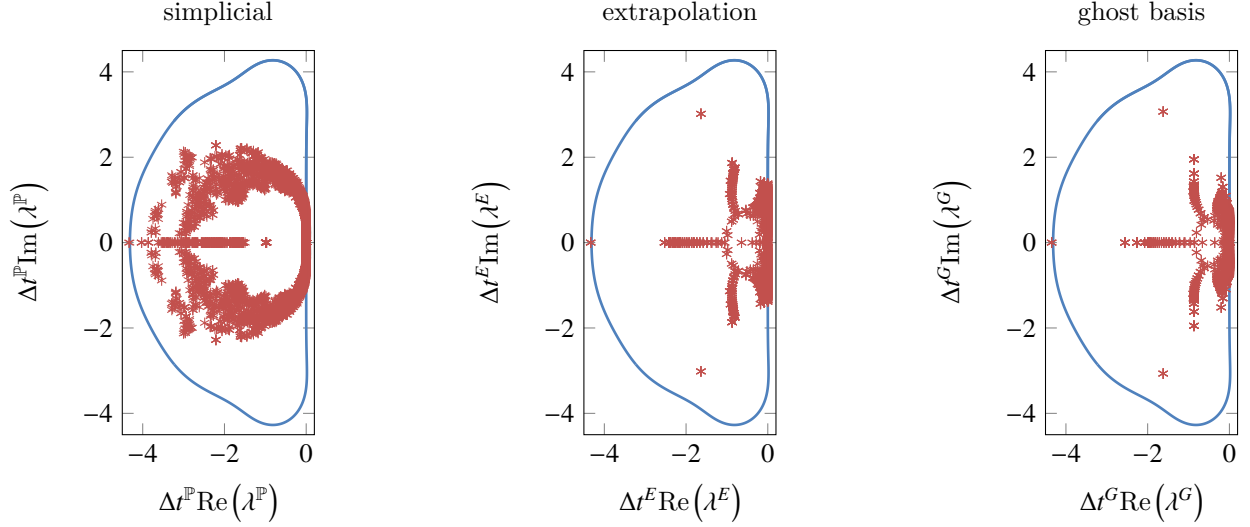


Figure 12: Time step scaled eigenvalue spectra for the methods with $n = 7$ along with the order 8 Taylor time integration stability region; see Table 2.

GD schemes, the eigenmode (not shown) associated with the time step restrictive eigenvalues has most of its energy at degrees of freedom at the corners of the element. We note that this phenomenon is multidimensional; in one space dimension the spectral radius of the GD differentiation matrices was found to be bounded independent of polynomial degree [1]. It is surprising that for a tensor product grid this property is not preserved, so the origin and, hopefully, suppression of the corner modes is a topic for future study.

Since the inverse of the time step is the number of steps required to complete a simulation, if the schemes are memory bandwidth limited the overall time to solution savings (as compared with the simplicial element method) is $(\Delta t^E/N_p^E)(N_p^P/\Delta t^P)$ for extrapolation GD and $(\Delta t^G/N_p^G)(N_p^P/\Delta t^P)$ for ghost basis GD. As can be seen in Table 2, both GD schemes are favorable in this metric. Additionally, in all cases except $n = 3$, the extrapolation method outperforms the ghost basis method.

5.5. Waves on a Disk

In this test we take Ω to be the unit disk and consider the analytic solution

$$p = \frac{\partial^2 u}{\partial t^2}, \quad v_x = \frac{\partial^2 u}{\partial t \partial x}, \quad v_y = \frac{\partial^2 u}{\partial t \partial y}, \quad (72)$$

with the function u being

$$u = \alpha \cos(R_0 t - \beta \theta) J_\beta(R_0 r). \quad (73)$$

Here $J_\beta(r)$ is the Bessel function of the first kind and (r, θ) are the polar coordinates of the Cartesian point (x, y) . In the test we use $\beta = 7$, choose R_0 so that $J'_\beta(R_0) = 0$ which ensures that the $\mathbf{n} \cdot \mathbf{v} = 0$ on the outer edge of the disk, and α is a normalization constant so that the energy in the solution is 1. For $n = 3, 5$, and 7 we choose R_0 to be the 2^{nd} root so that $R_0 \approx 12.93$ with $\alpha \approx 0.024$, and for $n = 9$ and 11 we choose R_0 to be the 5^{th} root so that $R_0 \approx 109.6$ with $\alpha \approx 0.0091$; both R_0 and α are determined numerically.

Here we consider three different methods for handling the disk geometry:

1. WADG on simplicial elements: base mesh of 48 simplicial elements,
2. WADG on simplicial elements coupled with GD: base mesh of 20 simplicial elements coupled with a central GD element in the center (see right panel of Figure 1), and
3. WADG-GD: 5 GD elements with the 4 edge elements being curved (see left panel of Figure 1).

n	GD coupled to WADG simplicial		WADG-GD	
	extrapolation N_0^E	ghost basis N_0^G	extrapolation N_1^E, N_2^E, N_3^E	ghost basis N_1^G, N_2^G, N_3^G
3	11	9	4, 6, 10	4, 6, 10
5	18	14	7, 10, 17	6, 9, 15
7	25	19	10, 15, 24	7, 10, 17
9	31	24	14, 20, 33	11, 16, 26
11	37	28	16, 23, 38	13, 19, 31

Table 4: GD parameters used for the disk test problem.

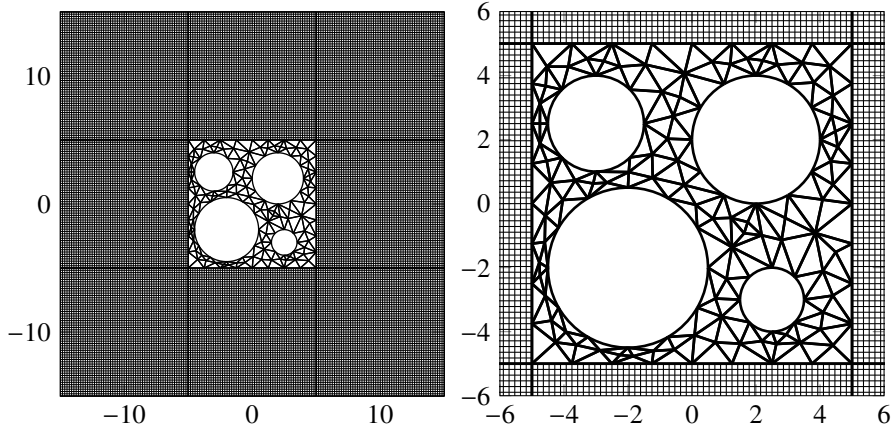


Figure 13: Computational mesh used for the inclusion test problem. (left) Full computational domain and base mesh. (right) Close up view showing the base simplicial mesh along with the GD-simplicial interface.

In the case of the purely simplicial mesh, the 20 elements around the edge of the base mesh match those in the right panel of Figure 1, e.g., the GD element is replaced with 28 simplicial elements.

For the coupled simplicial GD problem, the GD element has lower-left and upper-right corners $(\pm\sqrt{2}/2, \pm\sqrt{2}/2)$ and is discretized using an $(N_0 + 1) \times (N_0 + 1)$ grid of points, where N_0 for the extrapolation and ghost basis methods are given in Table 4. These parameters were chosen so that the coupled method has a lower error than the purely simplicial method at time $t = 2\pi\beta/R_0$ with the same n for refinement level 0 (with the exception of $n = 3$ where refinement level 1 is considered).

For the WADG-GD mesh, the center GD element has lower-left and upper-right corners $(\pm 1/3, \pm 1/3)$ and is discretized using an $(N_1 + 1) \times (N_1 + 1)$ interior grid. The outer elements have interior grids that are $(N_2 + 1) \times (N_3 + 1)$ where N_2 and N_3 are chosen so that the grid spacing along edges of the element are no larger than the grid spacing in the center element. The values for the extrapolation and ghost basis method used are given in Table 4, where the resolution is chosen in the same manner as for the coupled simplicial-GD element mesh.

Results for the disk test problem are given in Table 5 for $n = 3, 5, 7$ and in Table 6 for $n = 9, 11$. As can be seen all of the schemes perform as expected converging at high order.

An important question is whether the coupling of GD with simplicial elements has negatively affected the time step of the scheme. In Table 7 we give the maximum stable time step (determined as in Section 5.4) for each of the schemes. As can be seen, the coupled simplicial and GD schemes have similar time step restrictions as the pure simplicial method. Additionally, the benefits of handling geometry with smaller simplicial elements is clear from the increased time step as compared with the purely GD schemes; though we note that using more GD elements would likely improve the GD time step since the grid spacing could be made more uniform.

level	$n = 3$ error (rate)	$n = 5$ error (rate)	$n = 7$ error (rate)
WADG simplicial elements			
0	3.61×10^{-1}	6.08×10^{-3}	1.83×10^{-4}
1	9.20×10^{-3} (5.29)	1.01×10^{-4} (5.91)	8.36×10^{-7} (7.77)
2	4.61×10^{-4} (4.32)	1.65×10^{-6} (5.94)	3.41×10^{-9} (7.93)
3	2.89×10^{-5} (3.99)	2.61×10^{-8} (5.98)	1.37×10^{-11} (7.96)
WADG simplicial with extrapolation GD			
0	2.48×10^{-1}	5.63×10^{-3}	1.53×10^{-4}
1	7.79×10^{-3} (4.99)	9.33×10^{-5} (5.91)	6.86×10^{-7} (7.80)
2	4.80×10^{-4} (4.02)	1.54×10^{-6} (5.92)	2.82×10^{-9} (7.93)
3	3.03×10^{-5} (3.98)	2.46×10^{-8} (5.96)	2.38×10^{-11} (6.89)
WADG simplicial with ghost basis GD			
0	6.50×10^{-1}	6.05×10^{-3}	1.55×10^{-4}
1	7.65×10^{-3} (6.41)	1.19×10^{-4} (5.67)	6.84×10^{-7} (7.82)
2	4.08×10^{-4} (4.23)	2.44×10^{-6} (5.60)	2.83×10^{-9} (7.92)
3	2.54×10^{-5} (4.00)	5.72×10^{-8} (5.42)	1.64×10^{-11} (7.43)
WADG extrapolation GD			
0	1.05×10^{-1}	3.40×10^{-3}	1.16×10^{-4}
1	6.54×10^{-3} (4.00)	8.59×10^{-5} (5.31)	5.89×10^{-7} (7.62)
2	4.93×10^{-4} (3.73)	1.76×10^{-6} (5.61)	2.88×10^{-9} (7.68)
3	3.40×10^{-5} (3.86)	3.14×10^{-8} (5.81)	1.25×10^{-11} (7.85)
WADG ghost basis GD			
0	6.00×10^{-2}	3.37×10^{-3}	1.76×10^{-4}
1	2.21×10^{-3} (4.76)	1.82×10^{-4} (4.21)	1.06×10^{-6} (7.37)
2	1.40×10^{-4} (3.98)	3.40×10^{-6} (5.74)	5.10×10^{-9} (7.71)
3	9.22×10^{-6} (3.93)	7.75×10^{-8} (5.46)	2.19×10^{-11} (7.86)

Table 5: Disk results for $R_0 \approx 12.93$ and $\alpha \approx 0.024$.

level	$n = 9$ error (rate)	$n = 11$ error (rate)
WADG simplicial elements		
0	8.86×10^{-4}	4.15×10^{-5}
1	1.22×10^{-6} (9.51)	1.41×10^{-8} (11.52)
2	1.32×10^{-9} (9.85)	3.86×10^{-12} (11.84)
WADG simplicial with extrapolation GD		
0	7.10×10^{-4}	3.49×10^{-5}
1	9.57×10^{-7} (9.53)	1.14×10^{-8} (11.58)
2	1.06×10^{-9} (9.82)	7.07×10^{-12} (10.65)
WADG simplicial with ghost basis GD		
0	8.58×10^{-4}	3.96×10^{-5}
1	9.71×10^{-7} (9.79)	1.61×10^{-8} (11.27)
2	1.05×10^{-9} (9.85)	5.63×10^{-11} (8.16)
WADG extrapolation GD		
0	4.70×10^{-4}	3.57×10^{-5}
1	8.78×10^{-7} (9.07)	1.85×10^{-8} (10.92)
2	1.12×10^{-9} (9.61)	1.09×10^{-11} (10.72)
WADG ghost basis GD		
0	6.29×10^{-4}	4.23×10^{-5}
1	6.79×10^{-7} (9.86)	1.19×10^{-8} (11.80)
2	8.22×10^{-10} (9.69)	1.53×10^{-10} (6.28)

Table 6: Disk results for $R_0 \approx 109.6$ and $\alpha \approx 0.0091$.

n	Simplicial	Simplicial with extrapolation GD	Simplicial with ghost basis GD	extrapolation GD	ghost basis GD
3	3.4×10^{-2}	3.9×10^{-2}	3.9×10^{-2}	2.6×10^{-2}	1.3×10^{-2}
5	2.6×10^{-2}	2.8×10^{-2}	2.8×10^{-2}	1.5×10^{-2}	1.2×10^{-2}
7	1.8×10^{-2}	1.9×10^{-2}	1.8×10^{-2}	8.7×10^{-3}	7.0×10^{-3}
9	1.5×10^{-2}	1.6×10^{-2}	1.5×10^{-2}	6.5×10^{-3}	4.7×10^{-3}
11	1.1×10^{-2}	1.2×10^{-2}	1.2×10^{-2}	5.1×10^{-3}	4.0×10^{-3}

Table 7: Maximum stable time step for each of the schemes base mesh for the disk using the parameters in Table 4

5.6. Inclusion Scattering

As a final test we consider the scattering off of four cavity cylinders in an acoustic medium. The domain is of size 15×15 and the four cylinder centers (x, y) and radii R are

$$x_1 = 2, \quad y_1 = 2, \quad R_1 = 2, \quad x_2 = -2, \quad y_2 = -2, \quad R_2 = 2.5, \quad (74)$$

$$x_3 = -3, \quad y_3 = 2.5, \quad R_3 = 1.5, \quad x_4 = 2.5, \quad y_4 = -3, \quad R_4 = 1. \quad (75)$$

The computational mesh is shown in Figure 13. Around the four cylinders 240 simplicial elements are used and away from the cylinders 8 large GD elements are used; each of the GD elements is 5×5 and the region covered by simplicial elements is of size 5×5 . On the base mesh, each of the GD-simplicial interfaces has 8 simplicial elements and each of the GD elements uses an $(8n + 1) \times (8n + 1)$ interior grid; the GD grid spacing is thus $h = 5/8n$ in each direction. The outer and cylindrical inclusion boundaries are taken to satisfy the zero velocity boundary condition (2). For this test we consider polynomial orders $n = 5$ and $n = 7$ with GD elements using the extrapolation basis.

The initial condition is taken to be

$$p_0 = \exp(-2(r - 10)^2), \quad \mathbf{v}_0 = \mathbf{0}, \quad (76)$$

where $r = \sqrt{x^2 + y^2}$. This initial condition is a ring of radius 8 centered at the origin. The pressure field at times $t = 5, 10, 15,$ and 30 is shown in Figure 14. As can be seen the wave field becomes quite complex through the continued interaction with the cylinders.

Since we do not know the analytic solution for this problem, we assess the accuracy of the scheme through a self-convergence study. Namely, for a fixed n we run the solution at three resolutions; the mesh is refined as before using grid doubling for the GD elements and quadrisecting for the simplicial elements. We denote the solution on level l as $p^{(l)}, v_x^{(l)},$ and $v_y^{(l)}$, with level 0 being the base resolution and level 2 being the finest resolution. The convergence rate is estimated as

$$\text{rate estimate} = \log_2 \left(\frac{\Delta^{(1)}}{\Delta^{(2)}} \right), \quad (77)$$

$$(\Delta^{(l)})^2 = \frac{1}{2} \sum_{e \in \mathcal{E}} \int_{\hat{e}} J \left((p^{(l)} - p^{(l-1)})^2 + (v_x^{(l)} - v_x^{(l-1)})^2 + (v_y^{(l)} - v_y^{(l-1)})^2 \right). \quad (78)$$

We approximate the integral in (78) using the finest level's quadrature rule, namely the solutions from levels 0 and 1 are interpolated to the quadrature nodes of the level 2 mesh.

When this test is run with polynomial order $n = 5$ the estimated convergence rate is 6.3 and when $n = 7$ the estimated convergence rate is 7.5 at time $t = 30$.

6. Conclusions

In this paper we have shown how the Galerkin difference (GD) method can be used to efficiently handle complex geometries. Two approaches were considered: the use of curved GD elements with efficient handling of the mass matrix using the weight-adjusted approximation and the coupling with simplicial elements. In all cases the interface between elements can be nonconforming, meaning that different approximation spaces are used on the two sides of the interface. Semidiscrete energy stability was achieved through the use of a skew-symmetric discontinuous Galerkin formulation, with nonconforming interfaces handling using mortar elements. The scheme was observed to be high-order accurate in all of the test problems.

When coupling with simplicial elements, the results suggest that if there are K simplicial elements of order n along an interface the number of GD degrees of freedom along the interface should be roughly nK . We also observed that for a similar accuracy the GD method in general required fewer degrees of freedom than polynomial simplicial elements and that the allowed time step was larger. This suggests, that if implemented efficiently, GD can lead to a faster time to solution and that the scheme is good candidate for local time stepping.

One area for future work is the fact that in multiple dimensions, the GD scheme has a more restrictive time step than in one dimension. The modes restricting the time step are largely associated with the corners of the elements. This suggests that by modifying the GD basis near the corners of the element the time step might be improved.

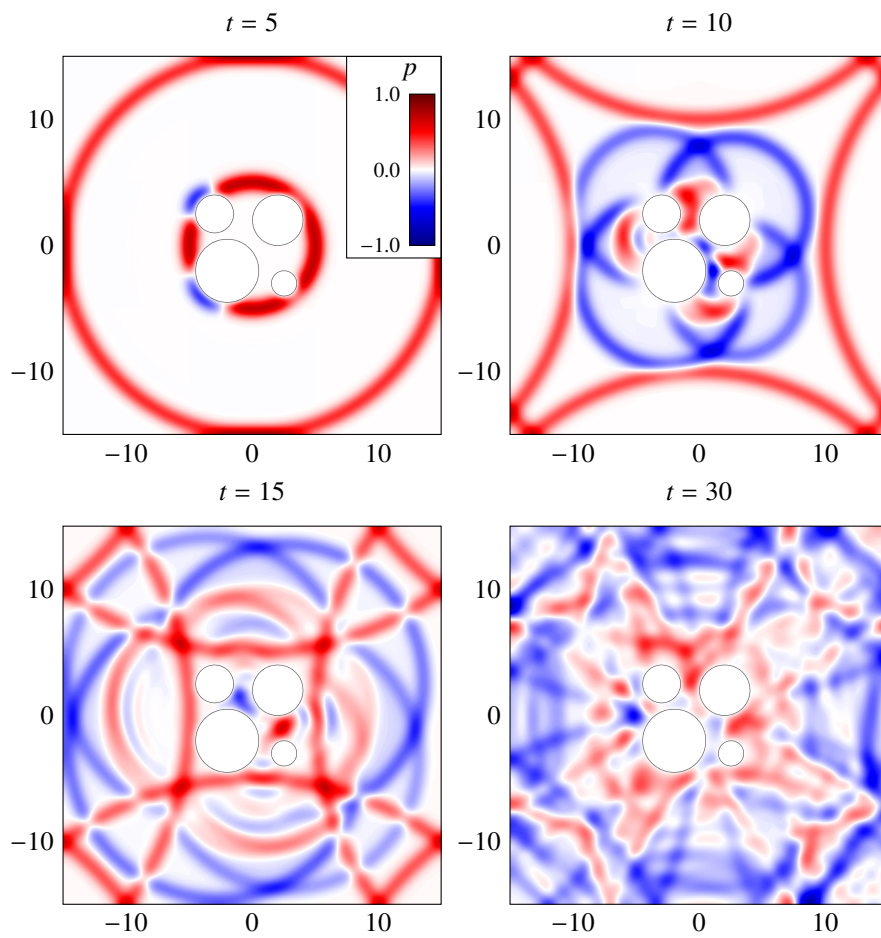


Figure 14: Computed pressure field solution for the inclusion problem. Solution is shown for $n = 5$ on the base mesh. The same saturated -1 to 1 color scale is used for all panels with the colorbar shown in the top-left panel.

Acknowledgments

Jeremy E. Kozdon was partially supported by National Science Foundation Award EAR-1547596 and Office of Naval Research Award N0001416WX01290. Computational resources were provided in part by National Science Foundation Award OAC-1403203.

Thomas Hagstrom was supported by contracts from the U.S. Department of Energy ASCR Applied Math Program and NSF Grant DMS-1418871. Any opinions, findings, and conclusions or recommendations expressed in this material are those of the authors and do not necessarily reflect the views of the Department of Energy or the National Science Foundation.

Jeffrey W. Banks was supported by contracts from the U.S. Department of Energy ASCR Applied Math Program, and by a U.S. Presidential Early Career Award for Scientists and Engineers.

Appendix A. Proof of Theorem 3.1

Taking the time derivative of (21) and substituting in (17)–(19) gives the following element energy dissipation rate

$$\frac{d\mathcal{F}^e}{dt} = \sum_{g \in \mathcal{G}^e} \Delta^{-g} \quad (\text{A.1})$$

where the mortar based energy rate of change is

$$\Delta^{-g} = -(\mathbf{p}^-)^T \mathbf{S}_J^g \mathbf{W}^g \mathbf{v}_n^* + (\mathbf{p}^-)^T \mathbf{S}_J^g \mathbf{W}^g \mathbf{v}_n^- - (\mathbf{v}_n^-)^T \mathbf{S}_J^g \mathbf{W}^g \mathbf{p}^*. \quad (\text{A.2})$$

Thus, the energy rate of change depends only on the energy rate of change across the mortar elements. To complete the proof we only need to consider a single mortar element g and show that energy does not increase across g . To do this we separately consider the case of g being a boundary mortar element and a mortar element between two elements.

If g is a boundary mortar element, then substituting in (6) for \mathbf{v}_n^* and \mathbf{p}^* with $p^+ = p^-$ and $v_n^+ = -v_n^-$ gives

$$\Delta^{-g} = -\alpha (\mathbf{v}_n^-)^T \mathbf{S}_J^g \mathbf{W}^g \mathbf{v}_n^-, \quad (\text{A.3})$$

which is non-positive if $\alpha \geq 0$ and \mathbf{S}_J^g is positive; note that \mathbf{W}^g is positive because the mortar quadrature is assumed to be a positive weight rule. Thus boundary mortars are energy non-increasing.

Recall that the mortar is partitioned such that g is a mortar element between two elements, e^- and e^+ . Since the flux and normal vectors are described from the viewpoint of an element, the two sides will use equal and opposite normal vectors. Using the normal of element e^- in the calculation for e^+ gives

$$\Delta^{+g} = (\mathbf{p}^+)^T \mathbf{S}_J^g \mathbf{W}^g \mathbf{v}_n^* - (\mathbf{p}^+)^T \mathbf{S}_J^g \mathbf{W}^g \mathbf{v}_n^+ + (\mathbf{v}_n^+)^T \mathbf{S}_J^g \mathbf{W}^g \mathbf{p}^*. \quad (\text{A.4})$$

With this, the energy rate of change across g is then

$$\Delta^{-g} + \Delta^{+g} = \llbracket \mathbf{p} \rrbracket^T \mathbf{S}_J^g \mathbf{W}^g \mathbf{v}_n^* + \llbracket \mathbf{v}_n \rrbracket^T \mathbf{S}_J^g \mathbf{W}^g \mathbf{p}^* + (\mathbf{p}^-)^T \mathbf{S}_J^g \mathbf{W}^g \mathbf{v}_n^- - (\mathbf{p}^+)^T \mathbf{S}_J^g \mathbf{W}^g \mathbf{v}_n^+. \quad (\text{A.5})$$

Using (6) as viewed from e^- for \mathbf{v}_n^* and \mathbf{p}^* , this becomes

$$\Delta^{-g} + \Delta^{+g} = -\frac{\alpha}{2} \llbracket \mathbf{p} \rrbracket^T \mathbf{S}_J^g \mathbf{W}^g \llbracket \mathbf{p} \rrbracket - \frac{\alpha}{2} \llbracket \mathbf{v}_n \rrbracket^T \mathbf{S}_J^g \mathbf{W}^g \llbracket \mathbf{v}_n \rrbracket, \quad (\text{A.6})$$

which is non-positive if $\alpha \geq 0$ and \mathbf{S}_J^g is positive. Thus energy is non-increasing across mortars between elements.

Since energy is non-increasing across all mortar elements g , we have that $\frac{d}{dt} \mathcal{F} \leq 0$ and the result $\mathcal{F}(t) \leq \mathcal{F}(0)$ for $t > 0$ follows upon integration.

Appendix B. Proof of Theorem 4.1

Using (51) it follows that

$$\mathbf{1}^T \mathbf{L}^T \mathbf{W} \mathbf{J} \mathbf{s}_y \mathbf{D}_s \mathbf{v}_y = \mathbf{x}_r^T \mathbf{L}^T \mathbf{W} \mathbf{D}_s \mathbf{v}_y = \int_{\hat{e}} x_r \frac{\partial v_y}{\partial s} = \int_{\hat{e}} \frac{\partial x}{\partial r} \frac{\partial v_y}{\partial s} = \int_{\hat{e}} J \frac{\partial s}{\partial y} \frac{\partial v_y}{\partial s}, \quad (\text{B.1})$$

where the second equality follows from the fact that the quadrature is exact for inner products and the third equality from the L^2 -projection (46). Similar calculations for the other metric terms yield:

$$\mathbf{1}^T \mathbf{L}^T \mathbf{W} \mathbf{J} \mathbf{r}_y \mathbf{D}_r \mathbf{v}_y = \int_{\hat{e}} J \frac{\partial r}{\partial y} \frac{\partial v_y}{\partial r}, \quad (\text{B.2})$$

$$\mathbf{1}^T \mathbf{L}^T \mathbf{W} \mathbf{J} \mathbf{r}_x \mathbf{D}_r \mathbf{v}_x = \int_{\hat{e}} J \frac{\partial r}{\partial x} \frac{\partial v_x}{\partial r}, \quad (\text{B.3})$$

$$\mathbf{1}^T \mathbf{L}^T \mathbf{W} \mathbf{J} \mathbf{s}_x \mathbf{D}_s \mathbf{v}_x = \int_{\hat{e}} J \frac{\partial s}{\partial x} \frac{\partial v_x}{\partial s}. \quad (\text{B.4})$$

Using this with the definitions of \mathbf{S}_x and \mathbf{S}_y gives

$$\mathbf{1}^T \mathbf{S}_x \mathbf{v}_x = \int_{\hat{e}} J \left(\frac{\partial r}{\partial x} \frac{\partial v_x}{\partial r} + \frac{\partial s}{\partial x} \frac{\partial v_x}{\partial s} \right) = \int_{\hat{e}} J \frac{\partial v_x}{\partial x}, \quad (\text{B.5})$$

$$\mathbf{1}^T \mathbf{S}_y \mathbf{v}_y = \int_{\hat{e}} J \left(\frac{\partial r}{\partial y} \frac{\partial v_y}{\partial r} + \frac{\partial s}{\partial y} \frac{\partial v_y}{\partial s} \right) = \int_{\hat{e}} J \frac{\partial v_y}{\partial y}. \quad (\text{B.6})$$

Putting these together we then have that

$$\mathbf{1}^T \mathbf{S}_x \mathbf{v}_x + \mathbf{1}^T \mathbf{S}_y \mathbf{v}_y = \int_{\hat{e}} J \left(\frac{\partial v_x}{\partial x} + \frac{\partial v_y}{\partial y} \right) = \int_{\hat{e}} S_J (n_x v_x + n_y v_y). \quad (\text{B.7})$$

Appendix C. Proof of Theorem 4.2

Appendix C.1. Constant Preservation

In order to show that constants are preserved, we let the solution be constant, i.e., for all $e \in \mathcal{E}$, $p = \beta$, $v_x = \gamma_x$, and $v_y = \gamma_y$ with $\beta, \gamma_x, \gamma_y \in \mathbb{R}$. Since the fields are the same constant across all mortar elements g , we have for each $g \in \mathcal{G}^e$ that $v_n^- = v_n^+ = n_x^- \gamma_x + n_y^- \gamma_y = \gamma_n^-$ and $p^- = p^+ = \beta$ and thus $v_n^* = \gamma_n^-$ and $p^* = \beta$. This, along with the fact that the $\mathbf{S}_x \mathbf{1} = \mathbf{S}_y \mathbf{1} = \mathbf{0}$ implies that (17)

$$\mathbf{M}_J \frac{dp}{dt} = \mathbf{0}. \quad (\text{C.1})$$

Considering now (18) we have that

$$\mathbf{M}_J \frac{dv_x}{dt} = \mathbf{S}_x^T \beta \mathbf{1} - \sum_{g \in \mathcal{G}^e} \beta (\mathbf{L}^g)^T \mathbf{n}_x^{-g} \mathbf{S}_J^g \mathbf{W}^g \mathbf{L}^g \mathbf{1}, \quad (\text{C.2})$$

In order to show that the right-hand side is zero we let $w \in V_h^e$ and multiply by w^T :

$$w^T \mathbf{S}_x^T \beta \mathbf{1} - \sum_{g \in \mathcal{G}^e} \beta w^T (\mathbf{L}^g)^T \mathbf{n}_x^{-g} \mathbf{S}_J^g \mathbf{W}^g \mathbf{1}^g = w^T \mathbf{S}_x^T \beta \mathbf{1} - \sum_{g \in \mathcal{G}^e} \beta (\mathbf{n}_x^{-g} w^-)^T \mathbf{S}_J^g \mathbf{W}^g \mathbf{1}^g. \quad (\text{C.3})$$

By Theorem 4.1 it follows that

$$w^T \mathbf{S}_x^T \beta \mathbf{1} = \int_{\hat{e}} S_J n_x w. \quad (\text{C.4})$$

and using this along with (54) we have that

$$\mathbf{w}^T \mathbf{S}_x^T \beta \mathbf{1} - \sum_{g \in \mathcal{G}^e} \beta (\mathbf{n}_x^{-g} \mathbf{w}^-)^T \mathbf{S}_J^g \mathbf{W}^g \mathbf{1}^g = 0. \quad (\text{C.5})$$

Since this must hold for all $w \in V_h^e$ it follows that

$$\mathbf{M}_J \frac{d\mathbf{v}_x}{dt} = \mathbf{S}_x^T \beta \mathbf{1} - \sum_{g \in \mathcal{G}^e} \beta (\mathbf{L}^g)^T \mathbf{n}_x^{-g} \mathbf{S}_J^g \mathbf{W}^g \mathbf{L}^g \mathbf{1} = \mathbf{0}. \quad (\text{C.6})$$

A similar calculation shows that

$$\mathbf{M}_J \frac{d\mathbf{v}_y}{dt} = \mathbf{0} \quad (\text{C.7})$$

and the scheme is constant preserving.

Appendix C.2. Conservation

In order to show that the scheme is conservative we multiply (17)–(19) each by $\mathbf{1}^T$ and sum over all elements. If the scheme is conservative, then the sum of each component should be zero. Considering first (17) we have that

$$\mathbf{1}^T \mathbf{M}_J \frac{d\mathbf{p}}{dt} + \mathbf{1}^T \mathbf{S}_x \mathbf{v}_x + \mathbf{1}^T \mathbf{S}_y \mathbf{v}_y = - \sum_{g \in \mathcal{G}^e} \mathbf{1}^T (\mathbf{L}^g)^T \mathbf{S}_J^g \mathbf{W}^g (\mathbf{v}_n^* - \mathbf{v}_n^-). \quad (\text{C.8})$$

Direct application of Theorem 4.1 and (54) then gives

$$\mathbf{1}^T \mathbf{M}_J \frac{d\mathbf{p}}{dt} = - \sum_{g \in \mathcal{G}^e} \mathbf{1}^T (\mathbf{L}^g)^T \mathbf{S}_J^g \mathbf{W}^g \mathbf{v}_n^*. \quad (\text{C.9})$$

Since, by construction, \mathbf{v}_n^* will be equal and opposite on the two sides of each mortar it follow that after summing over the whole mesh that

$$\sum_{e \in \mathcal{E}} \mathbf{1}^T \mathbf{M}_J \frac{d\mathbf{p}}{dt} = 0, \quad (\text{C.10})$$

and the pressure field p is conserved. Similarly, multiplying (18) and (19) by $\mathbf{1}^T$ gives

$$\mathbf{1}^T \mathbf{M}_J \frac{d\mathbf{v}_x}{dt} = - \sum_{g \in \mathcal{G}^e} \mathbf{1}^T (\mathbf{L}^g)^T \mathbf{n}_x^{-g} \mathbf{S}_J^g \mathbf{W}^g \mathbf{p}^*, \quad (\text{C.11})$$

$$\mathbf{1}^T \mathbf{M}_J \frac{d\mathbf{v}_y}{dt} = - \sum_{g \in \mathcal{G}^e} \mathbf{1}^T (\mathbf{L}^g)^T \mathbf{n}_y^{-g} \mathbf{S}_J^g \mathbf{W}^g \mathbf{p}^*, \quad (\text{C.12})$$

where we have used that $\mathbf{S}_x \mathbf{1} = \mathbf{S}_y \mathbf{1} = \mathbf{0}$. Summing over the whole mesh and using that the normal vectors are equal and opposite on both sides of the mortar elements gives:

$$\sum_{e \in \mathcal{E}} \mathbf{1}^T \mathbf{M}_J \frac{d\mathbf{v}_x}{dt} = 0, \quad (\text{C.13})$$

$$\sum_{e \in \mathcal{E}} \mathbf{1}^T \mathbf{M}_J \frac{d\mathbf{v}_y}{dt} = 0, \quad (\text{C.14})$$

thus the scheme conserves both the velocity components. Note that conservation of velocity does not require the use of Theorem 4.1 and (54), due to the use of the weak derivative.

References

- [1] J. Banks, T. Hagstrom, On Galerkin difference methods, *Journal of Computational Physics* 313 (2016) 310 – 327. doi:10.1016/j.jcp.2016.02.042.
- [2] J. Banks, T. Hagstrom, J. Jacangelo, Galerkin differences for acoustic and elastic wave equations in two space dimensions, *Journal of Computational Physics* (2018). doi:10.1016/j.jcp.2018.06.029.
- [3] J. Chan, Z. Wang, A. Modave, J. Remacle, T. Warburton, GPU-accelerated discontinuous Galerkin methods on hybrid meshes, *Journal of Computational Physics* 318 (2016) 142–168. doi:10.1016/j.jcp.2016.04.003.
- [4] T. C. Fisher, M. H. Carpenter, J. Nordström, N. K. Yamaleev, C. Swanson, Discretely conservative finite-difference formulations for nonlinear conservation laws in split form: Theory and boundary conditions, *Journal of Computational Physics* 234 (2013) 353–375. doi:10.1016/j.jcp.2012.09.026.
- [5] G. Gassner, A skew-symmetric discontinuous galerkin spectral element discretization and its relation to sbp-sat finite difference methods, *SIAM Journal on Scientific Computing* 35 (3) (2013) A1233–A1253. doi:10.1137/120890144.
- [6] D. A. Kopriva, G. J. Gassner, An energy stable discontinuous Galerkin spectral element discretization for variable coefficient advection problems, *SIAM Journal on Scientific Computing* 36 (4) (2014) A2076–A2099. doi:10.1137/130928650.
- [7] J. E. Kozdon, E. M. Dunham, J. Nordström, Simulation of dynamic earthquake ruptures in complex geometries using high-order finite difference methods, *Journal of Scientific Computing* 55 (1) (2013) 92–124. doi:10.1007/s10915-012-9624-5.
- [8] J. Nordström, Conservative finite difference formulations, variable coefficients, energy estimates and artificial dissipation, *Journal of Scientific Computing* 29 (3) (2006) 375–404. doi:10.1007/s10915-005-9013-4.
- [9] T. Warburton, A low-storage curvilinear discontinuous Galerkin method for wave problems, *SIAM Journal on Scientific Computing* 35 (4) (2013) A1987–A2012. doi:10.1137/120899662.
- [10] L. Friedrich, D. C. Del Rey Fernández, A. R. Winters, G. J. Gassner, D. W. Zingg, J. Hicken, Conservative and stable degree preserving SBP operators for non-conforming meshes, *Journal of Scientific Computing* doi:10.1007/s10915-017-0563-z.
- [11] J. Kozdon, L. Wilcox, An energy stable approach for discretizing hyperbolic equations with nonconforming discontinuous Galerkin methods, *Journal of Scientific Computing* doi:10.1007/s10915-018-0682-1.
- [12] J. Chan, R. J. Hewett, T. Warburton, Weight-adjusted discontinuous galerkin methods: Curvilinear meshes, *SIAM Journal on Scientific Computing* 39 (6) (2017) A2395–A2421. doi:10.1137/16M1089198.
- [13] J. S. Hesthaven, T. Warburton, *Nodal Discontinuous Galerkin Methods*, Springer New York, 2008. doi:10.1007/978-0-387-72067-8.
- [14] D. A. Kopriva, Metric identities and the discontinuous spectral element method on curvilinear meshes, *Journal of Scientific Computing* 26 (3) (2006) 301–327. doi:10.1007/s10915-005-9070-8.
- [15] J. Chan, J. A. Evans, Multi-patch discontinuous Galerkin isogeometric analysis for wave propagation: Explicit time-stepping and efficient mass matrix inversion, *Computer Methods in Applied Mechanics and Engineering* 333 (2018) 22–54. doi:10.1016/j.cma.2018.01.022.